

PICOSECOND TIME RESOLVED CATHODOLUMINESCENCE TO STUDY SEMICONDUCTOR MATERIALS AND HETEROSTRUCTURES

THÈSE N° 3960 (2007)

PRÉSENTÉE LE 30 NOVEMBRE 2007
À LA FACULTÉ DES SCIENCES DE BASE
LABORATOIRE D'OPTOÉLECTRONIQUE QUANTIQUE
PROGRAMME DOCTORAL EN PHYSIQUE

ÉCOLE POLYTECHNIQUE FÉDÉRALE DE LAUSANNE

POUR L'OBTENTION DU GRADE DE DOCTEUR ÈS SCIENCES

PAR

Samuel SONDEREGGER

ingénieur physicien diplômé EPF
de nationalité suisse et originaire de Grub (AR)

acceptée sur proposition du jury:

Prof. R. Schaller, président du jury
Dr J.-D. Ganière, directeur de thèse
Prof. C. Hébert, rapporteur
Prof. Y. Kawakami, rapporteur
Prof. F. Ponce, rapporteur



ÉCOLE POLYTECHNIQUE
FÉDÉRALE DE LAUSANNE

Suisse
2007

Abstract

A large number of characterization tools for semiconductor based heterostructures are available nowadays. Most of these techniques deliver high temporal resolution (down to hundreds of femtoseconds) or good spatial resolution (down to sub nanometer resolution), but not both simultaneously.

However, to get a complete picture of carrier recombination and diffusion processes in heterostructures, one needs a spectroscopic tool which simultaneously yields high temporal and spatial resolutions. The same kind of tool is also needed to obtain local excited carrier lifetimes in a disordered material.

Due to the need of such a characterization tool, we have developed an original picosecond time resolved cathodoluminescence (pTRCL) setup using an ultrafast pulsed electron gun mounted on a scanning electron microscope (SEM). The basic idea of the construction was to replace the original thermionic electron gun by a pulsed electron gun. Electron pulses are produced in the gun by the photoelectric effect: ultraviolet (UV) light pulses illuminate a gold photocathode which leads to electron extraction. This setup reaches simultaneous spatial and temporal resolutions of 50 nm and 12 ps, respectively.

Motivated by the exceptional luminescence efficiency of nitride based optoelectronic devices despite of the large defect densities, we first study local luminescence lifetime in the vicinity of threading dislocations (TDs) on GaN surface. We show that the effective luminescence lifetime decreases when approaching a TD. This variation is most probably due to the decrease of the non-radiative lifetime meaning that non-radiative recombination becomes predominant when approaching a dislocation.

We measure cathodoluminescence (CL) on InGaN based double quantum well (QW) structures. The structures are optimized to improve spatial resolution for monochromatic CL measurements. The study of these structures reveals the particular surface morphology of InGaN QWs by atomic force microscopy (AFM) and its connection to optical properties: The InGaN QW exhibits deep valleys oriented in the $\langle 1 - 100 \rangle$ directions where the QW thickness almost decreases to zero. TDs populate these valleys. pTRCL measurements show that excited carriers diffuse away from the TDs in the valleys which act as energy barriers hindering the excited carriers from non radiative recombination on the TDs. This possibly explains the high lu-

minescence efficiency of InGaN based heterostructures despite the high TD density.

Results on bulk BN samples are presented in the last chapter on experimental results. BN presents a very high bandgap, estimated around 6 eV , which makes optical excitation difficult in addition to a very high luminescence efficiency. These two properties make BN an ideal candidate for future UV lasers and light sources. Another exciting fact about BN is the possibility to synthesize multi- and single wall nanotubes. We show that the near bandgap luminescence peaks have very short lifetimes (between 20 ps and 32 ps) despite the indirect bandgap structure (theoretical prediction) of BN. Nevertheless, we associate the observed luminescence peak to direct exciton recombination of the Frenkel type.

Keywords: luminescence lifetime, cathodoluminescence, picosecond time resolved cathodoluminescence, nitrides, threading dislocations, heterostructures

Résumé

De nos jours, un grand nombre d'outils de caractérisation pour les hétérostructures à base de semiconducteurs sont disponibles. La plupart de ces techniques sont capables de délivrer soit une résolution temporelle élevée (quelques centaines de femtosecondes) soit une très bonne résolution spatiale (de l'ordre du nanomètre).

Cependant, pour comprendre les processus de diffusion et de recombinaison de porteurs de charge excités dans les hétérostructures, on a besoin d'un outil spectroscopique très performant en ce qui concerne la résolution spatiale mais aussi temporelle. De même, ce type d'outils est indispensable pour étudier les temps de vie de luminescence locaux dans un matériau désordonné.

Pour effectuer les études décrites plus haut, nous avons développé dans notre laboratoire un outil de caractérisation unique : la picosecond time resolved cathodoluminescence (pTRCL), employant un canon d'électrons pulsé ultrarapide. L'idée de base de la construction était de remplacer le canon à électrons thermionique original par une source pulsée d'électrons. Les pulses d'électrons sont générées en utilisant l'effet photoélectrique : un faisceau pulsé ultraviolet (UV) illumine une cathode d'or ce qui mène à l'extraction d'électrons. Cet outil est caractérisé par des résolutions spatiale et temporelle simultanées respectivement de 50 nm et 12 ps.

Motivé par le rendement de luminescence exceptionnelle des composés optoélectroniques à base de nitrures, malgré la densité de défauts très élevée, on étudie d'abord des temps de vie de luminescence locaux proches des dislocations à la surface (en anglais: threading dislocation ou TD) de GaN. On démontre que le temps de vie effective de luminescence décroît proche d'une TD en comparaison avec sa valeur dans le matériau massif. Cette variation est très probablement due à une diminution du temps de vie non radiative ce qui signifie que la recombinaison non radiative devient prédominante près d'une TD.

Nous mesurons ensuite la cathodoluminescence (CL) sur des doubles puits quantiques (QW) à base d'InGa_N, ces structures sont optimisées pour améliorer la résolution spatiale pour des mesures de CL monochromatiques. L'étude de ces structures démontre la morphologie de surface particulière de l'InGa_N par microscopie à force atomique (AFM) et montre sa corrélation avec les

propriétés optiques : les QW à base d'InGaN présentent des vallées profondes orientées selon la direction cristallographique $\langle 1 - 100 \rangle$ dans lesquelles l'épaisseur du QW est presque nulle et où la densité de TD est très élevée. Nos mesures pTRCL montrent que les porteurs excités diffusent hors des vallées ce qui prouve le caractère de barrière. Les porteurs excités ne peuvent donc pas se recombiner non radiativement sur les TDs, ce qui explique probablement le rendement de luminescence élevé des hétérostructures à base de GaN malgré la haute densité de TD.

Enfin, dans une dernière partie, nous exposons nos résultats expérimentaux obtenus lors de l'étude de nitrure de bore (BN) massif. BN présente une énergie de bande interdite élevée, d'environ 6 eV , combiné avec un rendement de luminescence important. Ces deux propriétés rendent le BN attractif pour la réalisation de lasers et de sources de lumière UV. Le BN reçoit aussi beaucoup d'attention de la part du monde scientifique grâce à la possibilité de pouvoir en synthétiser des nanotubes à parois multiples et uniques. On démontre que les pics de luminescence provenant de la région proche du gap fondamental ont des temps de vie très courts (entre 20 ps et 32 ps), malgré la nature indirecte de son gap fondamental tel que prévu par la théorie. Néanmoins on associe les pics de luminescence observés à la recombinaison d'Exciton de Frenkel directs.

Mots clés:

temps de vie de luminescence, cathodoluminescence, picosecond time resolved cathodoluminescence, nitrures, threading dislocations, hétérostructures

Zusammenfassung

Heutzutage existiert eine grosse Auswahl von Charakterisierungs Instrumenten für halbleiter-basierte Heterostrukturen. Diese Techniken zeichnen sich meist durch eine sehr hohe zeitliche (Femtosekunden) oder räumliche (Nanometer) Auflösungen aus, die jedoch nicht gleichzeitig erreicht werden können.

Um zu einem umfassenden Verständnis von Rekombination und Diffusion angeregter Ladungsträgern in Heterostrukturen zu gelangen, ist ein Instrument, das gleichzeitig hohe Raum- und Zeitauflösung liefert, unabdingbar. Derselbe Typ von Instrument wird auch für die lokale Ladungsträger Lebzeitmessung benötigt.

Daher haben wir ein einzigartiges Kathodolumineszenz Instrument mit Piko-sekunden Zeitauflösung (pTRCL) konstruiert. Die pTRCL basiert auf einer ultraschnellen, pulsierten Elektronenkanone, die wir auf ein Rasterelektronenmikroskop (SEM) angepasst haben. Die grundlegende Konstruktionsidee liegt in der Ersetzung der originalen, thermionischen Elektronenkanone durch eine pulsierte Kanone. Elektronenpulse werden durch den Photoelektrischen Effekt hergestellt: Ultraviolette (UV) Lichtpulse bescheinen eine Gold-Photokathode was zur Extraktion von Elektronen führt. Dieses Instrument erreicht simultan 50 nm räumliche, und 12 ps zeitliche Auflösung.

Motiviert durch die aussergewöhnlich hohe Lichteffizienz von Nitrid basierten Optoelektronischen Elementen, studierten wir zuerst lokale Lumineszenz Lebzeiten in der Nähe von Dislokationen (TD) an der Oberfläche von Galliumnitrid. Wir zeigen, dass die effektive Lumineszenz Lebzeit in der Nähe von TDs reduziert ist. Diese Änderung ist mit grosser Wahrscheinlichkeit einer Abnahme der nicht-radiativen Lebzeit zuzuschreiben. Dies bedeutet, dass nicht-radiative Prozesse in der Nähe von TDs dominieren.

Danach messen wir die Kathodolumineszenz (CL) von InGaN basierten doppel Quantentrog (QW) Strukturen. Die Strukturen sind für eine hohe Raumauflösung bei CL Messungen optimisiert. Die Messungen von diesen Strukturen decken die spezielle Oberflächen Morphologie von InGaN Quantentrögen durch Atomkraft-Mikroskopie (AFM) auf, und zeigen deren Zusammenhang mit den optischen Eigenschaften: Tiefe Täler, die parallel zu den $\langle 1-100 \rangle$ Richtungen verlaufen, kennzeichnen InGaN Quantentröge. Die Quantentrogdicke kann in diesen Tälern fast den Wert Null erreichen. Der

Grossteil der TDs befindet sich in diesen Tälern. pTRCL Messungen zeigen nun, dass angeregte Ladungsträger sich von den TDs in den Tälern, die als Energie Barrieren wirken, durch diffusion entfernen. Dadurch wird nicht-radiative Rekombination an TDs unterbunden. Dies liefert eine mögliche Erklärung der hohen Lumineszenz Effizienz von InGaN basierten Heterostrukturen trotz der hohen TD Dichte.

Resultate der Messungen an BN Proben werden im letzten Kapitel präsentiert. BN besitzt eine sehr hohe Bandlücke (6 eV), was die optische Exzitation schwierig macht. BN ist ebenfalls ein sehr effizienter Lichtemitter. BN ist Dank dieser genannten Eigenschaften ein idealer Kandidat für zukünftige UV Laser und UV Lichtquellen. Die Herstellung von BN nanotubes bietet zusätzliche, interessante Möglichkeiten. Wir zeigen hier, dass die Rekombination in Bandlückennähe, trotz deren indirekten Natur, sehr kurze Lebzeiten aufweist (zwischen 20ps und 32ps). Wir identifizieren die beobachteten Lumineszenz Zerfälle als direkte Frenkel Exziton Rekombination.

Schlüsselworte:

Lumineszenz Lebzeit, Kathodolumineszenz, Nitride, threading dislocations, Heterostrukturen, picosecond time resolved cathodoluminescence

Remerciements

En premier lieu, je tiens à remercier mon directeur de thèse, le Dr. Jean-Daniel Ganière, pour son soutien et son assistance au long de ce travail.

Je tiens également à remercier le Prof. Benoit Deveaud-Plédran pour m'avoir accueilli au sein de son laboratoire. Je lui remercie en particulier pour des nombreuses discussions scientifiques et les encouragements pendant ma thèse.

Je remercie le Prof. Nicolas Grandjean et le Dr. Eric Feltn pour leur disponibilité et pour une collaboration avec beaucoup de succès.

J'aimerais remercier le Dr. Michele Merano pour son travail excellent qui consistait à monter la pTRCL.

Un grand merci va aux deux post-docs: Dr. Stéphane Collin et Dr. Andrea Crottini qui ont suivi mon travail de recherche pendant deux ans. Je remercie en particulier le Dr. A. Crottini pour m'avoir appris des technique de spectroscopie optique et pour m'avoir assisté dans une phase critique du projet.

Je remercie également la Dr. Jelena Ristic qui est arrivé au laboratoire il y a quelques mois et qui a repris les mesures que j'avais commencées.

Je remercie le Dr. Rémy Sachot pour son aide précieuse avec certaines mesures.

Finalement, je tiens à remercier Mr. Hoan Nguyen d'OPEA pour son soutien et sa disponibilité pour résoudre des problèmes avec la pTRCL. Un grand merci aussi aux techniciens Roger Rochat et Nicolas Leiser pour leur assistance. Un grand merci va aussi à Hans-Jörg Bühlmann qui avait tout le temps une solution pour des problèmes techniques difficiles.

Contents

1	Introduction	1
2	Experimental Setup	3
2.1	Setup description and performance	3
2.2	Scanning Electron Microscope (SEM)	5
2.2.1	Pulsed photoelectron gun	7
2.2.2	Two photon excitation	10
2.2.3	xyz precision displacement system	12
2.3	Detection line	15
2.3.1	Quasi Continuous CL (CWCL) and secondary electron (SE) images	16
2.3.2	Time-resolved detection using the STREAK camera	16
2.3.3	Alternative Detection Line	18
3	Bulk GaN and InGaN based Quantum Wells	23
3.1	Properties of the III-Nitride materials	23
3.1.1	Structural properties	23
3.1.2	Band structure	29
3.1.3	Dislocations	30
3.2	Luminescence Lifetime measurement in the vicinity of TDs on GaN	33
3.3	TDs in InGaN Quantum Wells	44
3.3.1	Internal Electric Field	45
3.3.2	Effects of the Internal electrical field on optical properties	49
3.3.3	Sample Structure	52
3.4	Experimental Results	52
3.4.1	Continuous CL	52
3.4.2	AFM measurements	54
3.4.3	Correlation between CL and AFM measurements	58
3.4.4	pTRCL measurements	60

3.4.5	Discussion	61
3.5	Conclusion	65
4	Boron Nitride	69
4.1	Introduction	69
4.2	Experimental Results	70
4.3	Discussion	72
5	Conclusions and perspectives	77
5.1	pTRCL Setup	77
5.2	GaN and InGaN QW	77
5.3	Boron Nitrides	78
5.4	Perspectives	79
	Bibliography	80
A	Calculation methods	87
A.1	The transfer matrix method to evaluate hole and electron envelope functions in a QW	87
A.2	Calculation of the Excitonic Rydberg [1]	88
B	Technical drawings	91
B.1	Technical drawings of the xyz precision displacement system .	91
B.2	Technical drawing of the achromatic UV objective	91

1 Introduction

Ever since the 1970s the semiconductor industry is streaming towards smaller structures, presently reaching nanometer size. In parallel with the miniaturization in Si based IC technologies new 2D layer deposition technologies are developed that give rise to development of a whole new range of heterostructures that present new physical concepts and give rise to new devices. This miniaturization incited the development of new characterization tools, capable of accessing microstructures and, nowadays, even nanoobjects and their properties. In parallel with the development of semiconductor based heterostructures, new characterization tools have been developed. Nowadays, there are scanning probe microscopy (SPM) techniques like scanning electron microscopy (SEM) and atomic force microscopy (AFM) which are routinely used to characterize surface morphology of nanostructures. These techniques offer resolutions down to 1 nm for an SEM and sub-nanometer for the AFM. Optical techniques like scanning near-field optical microscopy (SNOM) or micro photoluminescence (PL) are used to assess fundamental physical properties of nanostructures. Thanks to the introduction of easy to use pulsed laser systems, optical methods yield very high temporal resolution, of some hundreds of femtoseconds. Such high temporal resolution is essential for studying nanostructures since luminescence phenomena in such structures often occur on picosecond to femtosecond timescales. On the other hand, the spatial resolution of optical tools is often limited by the diffraction limit. The ideal measurement tool for nanostructures would be the one able to combine the high spatial resolution of a SPM techniques with the high temporal resolution of optical techniques. These ideas were behind the initiation of the picosecond Time Resolved Cathodoluminescence (pTRCL) project by Dr. J.-D. Ganière in 2001. The continuous electron gun of a standard SEM was replaced by a new pulsed electron gun. Electron pulses are generated by the photoelectric effect in a gold photocathode using UV laser pulses. To obtain high temporal resolution, the cathodoluminescence signal is analyzed with a streak camera. The development of the setup was finished in 2004. The demonstration of its performance was achieved by transport measure-

ments on InGaAs/AlGaAs/GaAs micropylamids [2, 3] grown in the group of E. Kapon at EPFL. The pTRCL setup is characterized by simultaneous spatial and temporal resolutions of 50 nm and 12 ps, respectively.

The main objective of this thesis work is to use the pTRCL setup to investigate GaN based nanostructures. Since Nakamura *et al.* reported the first candela-class blue light emitting diode (LED) in 1994 [4], GaN based nanostructures have been the subject of intense research efforts due to their increasing importance in optoelectronics. These structures present very high luminescence efficiencies despite high defect densities, which has been an important puzzle over the last years. These high defect densities are introduced due to the lack of lattice matched substrates for GaN. GaN based nanostructures are very inhomogeneous which implies that one needs a local probe to assess its properties. With the goal to better understand the effects which lead to the high luminescence efficiency, local pTRCL lifetime measurement on InGaN based quantum wells (QW) and on bulk GaN were carried out. We also demonstrated that the pTRCL setup can be used to study high bandgap semiconductors such as boron nitride (BN). We detected time resolved signal up to energies of 5.77 eV (215 nm). BN is a very interesting material since it can be synthesized in the form of nanotubes and its high luminescence efficiency and high bandgap makes it an ideal candidate for UV light sources and UV laser.

This work is organized in the following way: We start by introducing and explaining the pTRCL technique. In the experimental part, we will first discuss the particularities of GaN and GaN or III-nitrides based heterostructures before we present and discuss the results obtained on bulk GaN and on InGaN based QWs. After this, the results obtained on BN are presented and discussed. We will end by a general conclusion and by discussing some perspectives of the pTRCL technique.

2 Experimental Setup

In the first section of this chapter a general description of the Picosecond Timeresolved Cathodo-Luminescence (pTRCL) setup will be given explaining how the three main components, pulsed laser, electron microscope and the detection line, are combined to work together in the pTRCL setup. The succeeding sections expose the parts of the different components in a detailed way.

2.1 Setup description and performance

The central part of our setup is a JEOL 6360 scanning electron microscope (SEM) in which the original tungsten source was replaced by an optically driven pulsed electron gun with high brightness. The electron pulses are produced by the photoelectric effect in a 20nm thick gold film evaporated on a fused silica window. The energy spread δE of the electron pulses is estimated to be $\delta E \approx 100\text{meV}$ ([5]). The photocathode is backilluminated by 150fs UV laser pulses centered around $\lambda = 266\text{nm}$ at a repetition rate of 80MHz . The energy of the exciting photons is above the gold workfunction $\phi \approx 4.2\text{eV}$ (depending on the crystallographic orientation [6]) thus ensuring a quantum efficiency of 3.8×10^{-6} . The UV laser pulses are generated through third-harmonic generation. The fundamental beam is produced by a standard Ti:Sapphire oscillator¹. These optically generated pulses are then focused on the sample surface using the SEM column's electro magnetic lenses. We usually work with an average power of $P_{av} \approx 100\text{mW}$ at the exit of the third-harmonic generation system. The sample is mounted on top of a motorized xyz precision displacement system using piezoelectric motors. The sample holder is connected through a copper braid to a liquid nitrogen reservoir. At the present, we are testing a liquid helium cryostat adapted for our microscope and developed in collaboration with Janis, Inc. Luminescence emitted from the sample is collected with a parabolic mirror and coupled

¹Coherent Mira 900 F/P pumped by a Coherent Verdi 8W

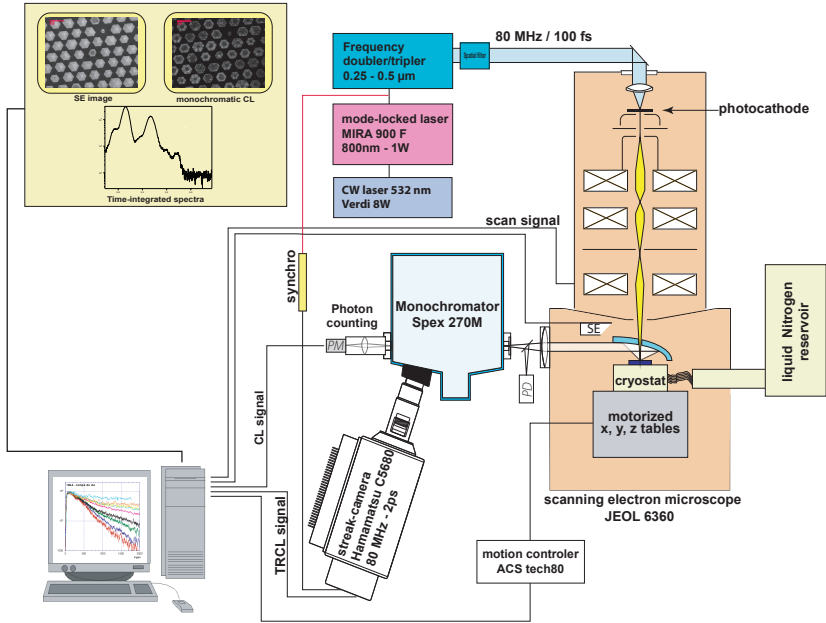


Figure 2.1: Picosecond Time-Resolved Cathodoluminescence (pTRCL) setup.

into a monochromator in order to disperse the signal energetically. The monochromator has two exit ports: one for the streak camera, for time-resolved measurements, and another one with a photo-multiplier, used in the photon counting mode, to record quasi continuous cathodoluminescence² (CL) maps. A second photo-multiplier operated in continuous mode offers the possibility to register polychromatic CL maps directly at the optical exit of the microscope, independently of the alignment of any optical component after the microscope.

A photograph of the described setup is shown in figure 2.2.

²By quasi-continuous we mean that sample excitation takes place in pulsed mode but the detection is continuous. The abbreviation CL always designs quasi-continuous mode unless stated otherwise.

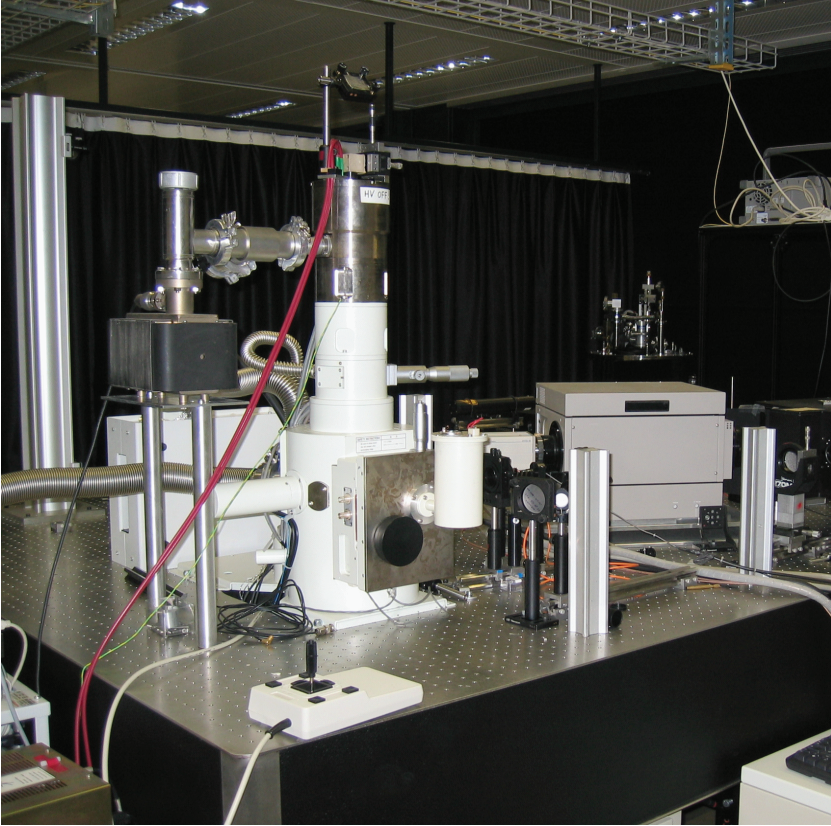


Figure 2.2: The pTRCL setup in our lab.

2.2 Scanning Electron Microscope (SEM)

A standard SEM column images the electron source (smallest beam cross-section at the source or crossover) on the sample surface with a demagnifica-

tion factor M varying approximately from $M = 10$ to $M = 5000$ depending on the type of the used electron source.

The diameter of our electron source corresponds to the size of the focused laser spot on the cathode surface which has a typical full width at half maximum (FMWH) of $3\,\mu\text{m}$. This means that we were obliged to choose an SEM column with $M \approx 1000$ to get nanometer resolution. Such SEM columns usually use a thermionic emission gun based on a heated tungsten hairpin. On the other hand our pulsed electron gun works like a field emission gun (FEG) usually consisting of two anodes: the first anode extracts the electrons from the metal and the second anode accelerates the electrons to the final kinetic energy. This means that our FEG like electron source needs electron optics adapted to a thermionic emission gun.

Finally, a JEOL 6360 SEM with a tungsten hairpin filament was chosen for the pTRCL setup. The acceleration voltage can be varied between $1\,\text{kV}$ and $30\,\text{kV}$ and the anode is grounded. An electromagnetic two-stages deflection unit is employed to align the electron beam before entering the microscope optical column.

The first microscope lens is an electromagnetic 2-stages zoom condenser lens system that performs beam demagnification. A conical objective lens focuses the electrons on the sample. The optimal working distance is $8\,\text{mm}$. Three objective lens aperture pinholes ($100 - 30 - 20\,\mu\text{m}$) can be inserted in the electron beam paths. The smallest one is used for high resolution observation. The scan coils deflectors allow for image magnifications from 30 to 300000. An astigmatism correction system is also provided.

The microscope is equipped with an Everhart-Thornley detector for secondary electron (SE) imaging mode operation. The guaranteed microscope resolution in SE mode is $3\,\text{nm}$ under ideal conditions³.

The SEM electronics were separated from the column which was mounted on an optical table to avoid difficulties with the optical alignment. Usually we use the standard JEOL software to align the microscope column and to get the optimal resolution. However, as far as scan speed is concerned, the

³acceleration voltage of $30\,\text{kV}$; $8\,\text{mm}$ working distance

JEOL software is very limited, allowing only for three different settings with $68\ \mu\text{s}$ dwell time per pixel for the slowest, which is often not slow enough. For this reason we connected an external scan generator, fabricated by the company 4pi Analysis, to the microscope, dwell times of the electron beam per pixel can be adjusted between $1\ \mu\text{s}$ per pixel up to $800\ \mu\text{s}$. More details can be found below in the section devoted to the detection line.

2.2.1 Pulsed photoelectron gun

The electron gun implemented in our setup was developed in close collaboration with the french company OPEA in Paris. The gun is isolated from the SEM column by an additional valve and pumped by a ionic pump (Varian VacIon Plus 25) to achieve high vacuum conditions at an approximate pressure of $5 \times 10^{-7}\ \text{mbar}$.

UV pulses are focused on the cathode surface by a UV microscope objective optimized for a wavelength of $266\ \text{nm}$ with a $8.5\ \text{mm}$ working distance. The objective is at the cathode potential to avoid electrical discharges and it is connected to a xyz linear stage through a delrin isolation block. The cathode consists of a $300\ \mu\text{m}$ thick fused silica window on which we evaporate a $20\ \text{nm}$ thick gold film. The extraction anode (pinhole) is mounted at a small distance ($2\ \text{mm}$) from the cathode. The voltage applied between the cathode and the pinhole can be varied between $-1\ \text{kV}$ and $-30\ \text{kV}$. When the valve is open, a Faraday cup can be inserted to measure the emitted current at the cathode level for alignment purposes. A photo of the gun is shown in figure 2.3. A series of test measures were made on a gun prototype before the actual electron gun could be constructed. An extensive report of the test setup and results can be found in chapter 3 of Michele Merano's PhD thesis work [5], who realized the main developments of the system. The optical properties of the gun are also reported in this work and an abbreviated version can be found in reference [7]. Here, we will limit ourselves with a summary of the main properties of the pulsed photoelectron gun.

The spatial resolution [5] in SE mode has been estimated to be $50\ \text{nm}$ according to the study of a sample consisting of gold particles deposited on an amorphous carbon film. It corresponds to the distance over which the contrast of the image of a gold particle border varies from 90 % to 10 % (see figure 2.4). Such a value is in good agreement with what can be estimated from the brightness of our photocathode. The axial brightness β and influ-



Figure 2.3: Photo of the electron gun. Dimensions: 23 *cm* in height and 12 *cm* in diameter.

ence of space charge effects were measured on the gun prototype. We find $\beta = 1.8 \times 10^3 \text{ A/cm}^2 \text{ sterad}$ at an acceleration voltage of 20 *kV*. This value is typically 100 times smaller than that of modern thermionic electron guns yielding a typical resolution of 3 *nm*. This means that there is still enough current within a spot with a diameter of 3 *nm* to record secondary electron images. With our gun, we manage to have the same current in a spot ten times bigger meaning that we can expect a maximal resolution around 30 *nm*. The 50 *nm* resolution is further degraded due to the parabolic mirror, that obliges us to use a working distance of 12 *mm* which is not optimal for the microscope. This results in difficulties when focussing the beam on the sample surface. Moreover, the parabolic mirror also absorbs a portion of the secondary electron signal thus decreasing the signal to noise ratio of the

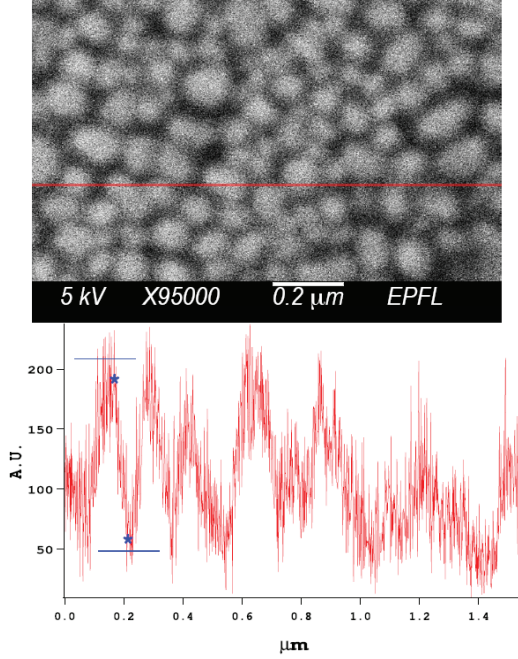


Figure 2.4: Pulsed SEM image of gold particles on a carbon film.

Everhardt Thornley detector.

Space charge effects refer to the longitudinal and transverse broadening of an electron packet due to Coulomb repulsion between the charged particles. There are several reports [8, 9, 10, 11, 12] describing the case of electron pulse broadening during propagation due to space charge effects. In our case, there clearly is transverse broadening of the electron pulses: cathode current is around 40 nA but we only have 10 pA (corresponding to one electron per pulse) probe current at the sample level which signifies that 99.9 % of the electrons are stopped by intermediate pinholes. Longitudinal broadening directly influences the temporal resolution of the system. The cathode is excited by 150 fs long pulses and we measure 12 ps long electron pulses. Since

the photon-electron conversion at the cathode is quasi instantaneous[13], this fact can only be explained by space charged induced broadening. The 3D mean field analysis we used to explain the results on the gun prototype[12] clearly shows that coulomb repulsion between the electrons has to be taken into account for typical electron densities up to $50/pulse/\mu m^2$ on the cathode level of our gun.

2.2.2 Two photon excitation

Using single photon excitation has the advantage of being very efficient. However, creating photons at 4.65 eV implies the use of an optical third-harmonic (or even higher harmonic) generation system (THGS). In the THGS we use, the laser pulse passes first through a 1.5 mm thick LBO crystal for second harmonic generation and then through a 0.5 mm thick BBO crystal for third harmonic generation. Thus the spatial profile of the laser pulse at the exit of the THGS is far from being gaussian and has to be filtered. We use a spatial filter with a $10\text{ }\mu m$ diameter pinhole which cleans the beam but cuts more than 90% of the power. As a result we work at typical average powers of 10 mW . The photocathode transmits 10% of the incoming light into the microscope's column. This stray light adds additional noise to the signal and can make signal detection impossible if the signal energy overlaps with the UV pulse energy. The optical components (lenses, mirrors, fibers etc.) that work at 4.65 eV have also to be chosen very carefully and are usually more expensive than standard optical components made out of BK7 glass, which exhibits a sharp cutoff for energies higher than 3.5 eV .

Due to these described drawbacks, it would be advantageous to work with lower energy pulses. This means that electrons inside the cathode have to be excited via a multi-photon process. We tested two photon excitation with our gun using the second harmonic output of the THG at 3.1 eV and an average power of 22 mW . The quality of the output beam is considerably better since the laser pulses pass only through the LBO crystal.

Figure 2.5 shows a secondary electron (SE) image obtained by exciting the cathode with a two-photon process. There is no difference between SE images obtained by single- and two-photon excitation. It would be preferable to work in the two-photon excitation scheme since the alignment of the optical system is easier and stays more stable over time. In addition, since we reach a 30 % efficiency for second harmonic generation, we could work at higher

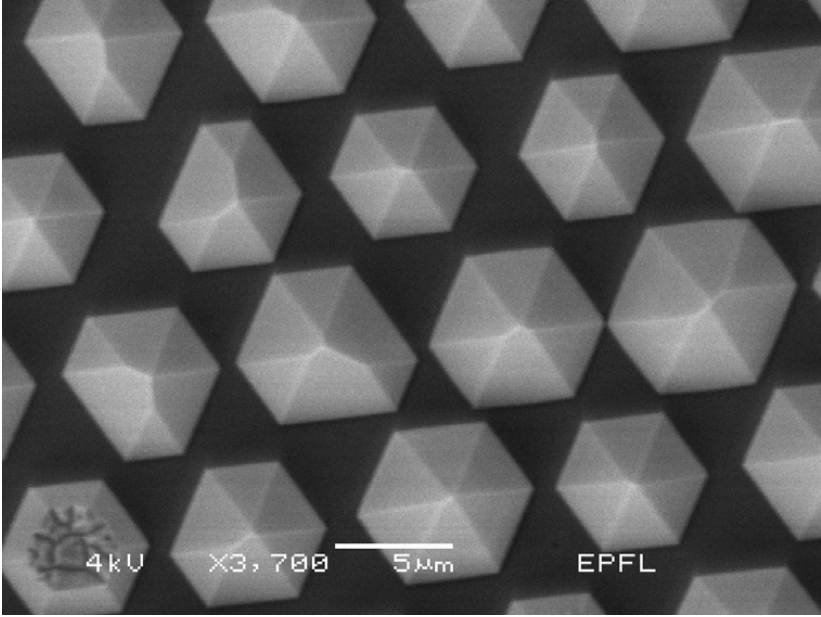


Figure 2.5: SE mode image of GaN micropylramids. The cathode is excited with photon energies below the gold workfunction.

probe current thus improving the signal to noise ratio in all imaging modes and probably spatial resolution as well.

There's a fundamental reason why we chose to work with a single-photon excitation: Two photon excitation at 3.1 eV can overlap with the energy of the main emission peak of the *InGaN/GaN* quantum wells studied during the elaboration of this thesis.

One could also try getting rid of the transmitted light subtraction of on and off sample spectra. The difficulty with this method is that the reflection of the light might change when moving off the sample which would introduce errors in the subtraction.

For these reasons we chose to carry out all measures using the third harmonic

to excite.

2.2.3 xyz precision displacement system

One of the basic issues in CL is the light collection using a parabolic mirror. The exciting electron beam should arrive on the sample surface at the focal spot of the mirror. In the experiment, when the beam is swept over a surface of approximately $10 \times 10 \mu\text{m}^2$ one already starts to notice intensity variations due to misalignment. Thus it is advantageous to work with a beam focused at the correct position, and to move the sample with an xyz precision displacement system working in closed loop mode to be able to verify the position. The system should have the following properties:

- speed up to several mm/s
- adapted for vacuum of at least 10^{-6} mbar
- high precision, of the order of microscope resolution (i.e. 50 nm)
- no jitter
- non magnetic
- high mechanical stability to avoid vibrations in a compact design

Such a system was not commercially available at the time we needed it so we chose to construct it in collaboration with the Swiss company Bytics located in Uster. The final system is depicted in figure 2.6. It contains precision mechanics from Sulzer-Inotech, piezoelectric motors from Nanomotion, optical position encoder from Numerik Jena and is controlled by a Spyii+ controller from ACS Tech 80. Piezoelectric motors possess all the properties cited above. The piezoelectric effect in piezoceramics refers to conversion of electrical field into mechanical strain. Under adequate electrical excitation drive the piezoceramic element can be caused to simultaneously undergo longitudinal extension and transverse bending. By choosing an adapted geometry, the simultaneous excitation of the longitudinal extension mode and the transverse bending mode creates a small elliptical trajectory of the piezoceramic element. Stage movement will occur as a result of friction between the stage and the piezoceramic element, when these two are put close enough to be in contact. A ceramic stripe glued on the stage (see figure 2.7) ensures

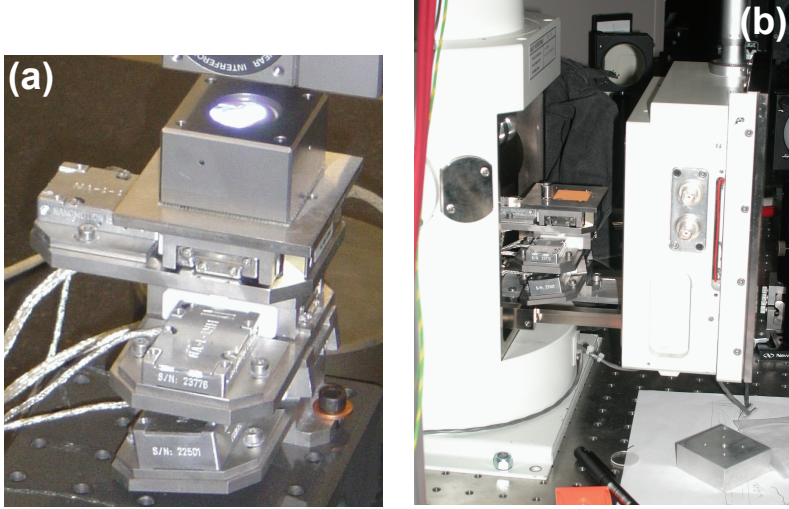


Figure 2.6: Photographs of the xyz displacement system mounted on a reference interferometer to verify the precision (a) and in our microscope (b). Dimensions: $13.5 \times 13.5 \times 7.7 \text{ cm}^3$, lwh

good contact between the piezoceramic element and the stage. The periodic nature of the driving force allows continuous smooth motion for unlimited travel. If no voltage is applied to the motor, the position is kept stable by the stiffness of the piezoceramic element. Position is recorded by optoelectronic position sensors from Numerik Jena GmbH. Figure 2.8 shows a scheme of the working principle of the detectors. The ruler is glued on the precision stage and has, in our case, a grating with $20\mu\text{m}$ spacing between the lines. The detector head contains an infrared light emitting diode (LED) mounted behind a transparent glass substrate on which a second grating with a different spacing is deposited. The infrared sensor is also mounted behind the glass substrate. Infrared light emitted from the LED is reflected on the ruler and passes through the second grating before being detected. The passage through the gratings yields a Moiré pattern on the detector with moving fringes when the stage moves[14]. Interpolation of the measured signal yields a detector resolution of $0.05\mu\text{m}$. The Spii+ controller board sends the sig-

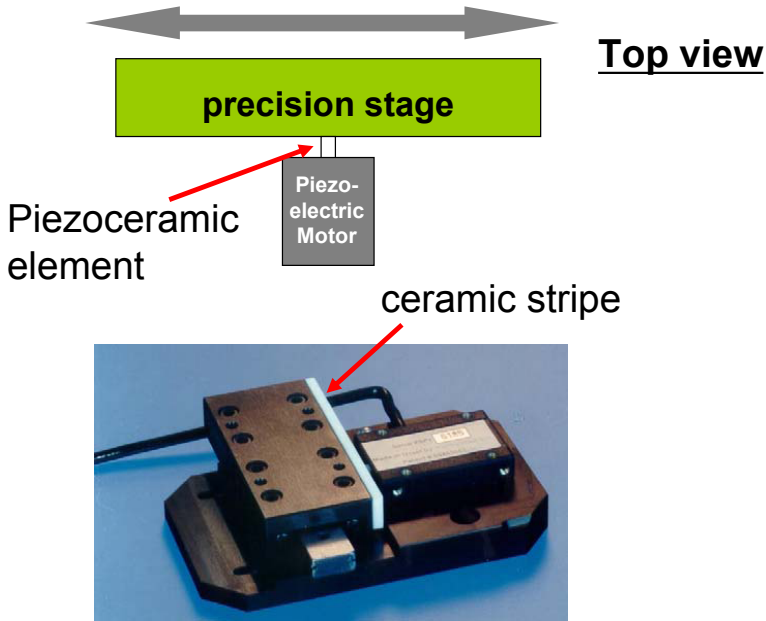


Figure 2.7: The upper part of the figure illustrates the coupling between the piezoceramic element and the precision stage. A photo of a piezoelectric motor coupled to a precision stage is depicted on the lower part of the figure.

nal to the motor driver and reads the position feedback from the position sensors. The three axes of the stages can be moved directly by a joystick or any movement can be easily programmed in ACSPL+, the programming language from ACS Tech 80. The stand alone controller unit is connected to the network using the TCP/IP which allows easy access to the board memory from any computer.

We can sweep the sample in the xy plane over a travel range of 2 cm in each direction. To displace the sample in height and to keep maximal stability we chose to move the z stage on a inclined plane by 10 degrees. The unwanted

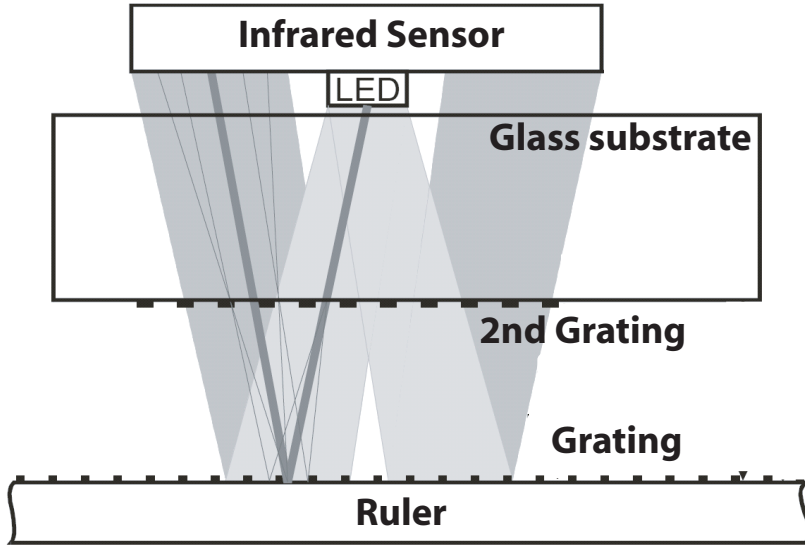


Figure 2.8: Operating principle of a distance measurement sensor.

displacement in the y direction when the height is changed is compensated automatically by virtually connecting the z and y axes through the controller. The maximum travel in z is limited to 2 mm . Technical drawings of the stage can be found in the appendix.

2.3 Detection line

The light emitted from the sample is collected and collimated using the parabolic mirror. After reflection on two broadband mirrors the luminescence is focused on the entrance slit of a Spex 270M imaging monochromator using an achromatic UV objective from B. Halle Nachfl. Optik in Germany (technical drawings of this objective can be found in the appendice). The objective's diameter and focal distance are chosen to fit the monochroma-

tor entrance aperture ratio of $f/4$. The imaging monochromator we use is constructed in a standard Czerny-Turner geometry with a focal length of 27 cm . We usually work with a 600 grooves/mm grating blazed at 400 nm . The spectral dispersion for this grating is given as 1.6 nm/mm . We typically work with an entrance slit width of $250\text{ }\mu\text{m}$ yielding a passing bandwidth of 0.5 nm (image magnification of 1.23 in the monochromator).

2.3.1 Quasi Continuous CL (CWCL) and secondary electron (SE) images

In order to record CL signal from the photomultiplier and SE signal from the Everhardt Thornley detector an external scan generator unit from 4Pi (Spectral Engine II, software version v 1.5.6) was used. This unit controls the electron beam position, (x, y) , on the sample and records up to four signals in parallel, $I(x, y)$ for each position. Then the software maps the function $I(x, y)$ using 2^8 (eight bits) or 2^{16} (sixteen bits) grey levels. The 4Pi external scan control can also be used to register other signals like EELS, X-ray, etc.. Cathodoluminescence signal is recorded by a H7732P-01 photon counting photomultiplier (PM) from Hamamatsu Photonics. This PM is optimized for UV signals in the range of 185 nm to 680 nm . The current pulses from the PM are fed into a charge sensitive preamplifier-discriminator (A-101 from Amptek) which converts them into 5 V TTL pulses with a length of 220 ns . The pulse counter in the external scan unit works up to a frequency of $\approx 300\text{ kHz}$ and the adjustable dwell time per pixel goes from $1\text{ }\mu\text{s}$ to 16 s . We work with typical dwell times per pixel of a few milliseconds and signal level of $\approx 100\text{ counts/pixel}$.

2.3.2 Time-resolved detection using the STREAK camera

Time resolved detection is achieved by using a Universal Streak Camera C5680 from Hamamatsu Photonics K.K. In general, Streak cameras convert temporal information into spatial information by using a time-dependent electric field. Figure 2.9 shows the operating principle of a streak camera. The photocathode converts the luminescence signal into an electron pulse which is deviated between the deflection plates. The variable electric field is generated by applying a sine wave form voltage on the deflection plates having the same frequency as the pulsed laser repetition rate (synchronisation signal). The deviated electrons are amplified in the multi channel plate

(MCP) and are converted back into photons on the phosphor screen behind which a charged coupled device (CCD) is mounted. Detection takes place

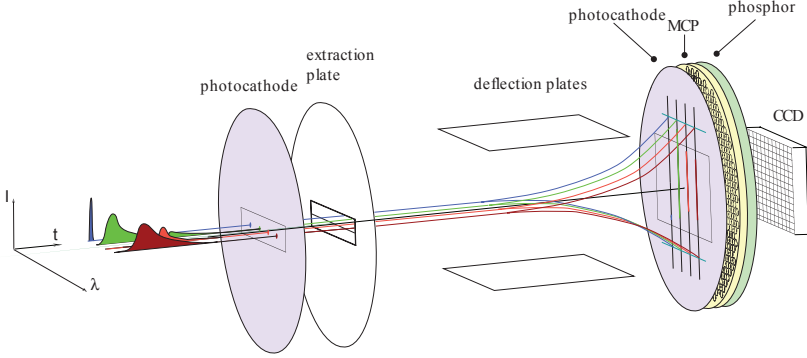


Figure 2.9: Operating principle a streak camera.

only during the almost linear like of the electric field generating sine wave. It becomes clear that the aperture of the temporal (horizontal) slit directly influences the time resolution. The intrinsic time resolution of the Streak camera is $2ps$ according to the specifications given by the manufacturer. This resolution is limited by the jitter introduced by the electronics between the synchronisation signal and the variation of the time-dependent electric field. One can choose between several time ranges when working with the streak camera. To reach maximum temporal resolution one should work in the fastest time range ($0 - 150ps$) and close the temporal slit to a few micrometers. However, in our setup the time resolution is not limited by the streak camera but by the electron pulse length (see discussion below). When it comes to temporal range, we can accurately measure maximal signal durations of $2ns$. This limit is imposed by the laser repetition rate.

Raw data from the Streak camera consist of two-dimensional maps of $1024 \times 1024 pixel^2$. Over the wavelength range covered by the Streak Camera, pixel number px on the horizontal axes is proportional to the wavelength, λ : $\lambda = px\alpha + \lambda_0$, where the factor α and the offset λ_0 can be determined by using a spectral calibration lamp to illuminate the monochromator entrance

slit. The pixel number on the vertical axes is proportional to time and the calibration factors are given by the Streak camera manufacturer. The point zero on the time axes can be chosen with an arbitrary offset. Intensities are color coded with an arbitrarily chosen color scale.

The temporal resolution of the setup was determined by fitting a time resolved luminescence signal from a bulk GaN sample. Our results are best fit by supposing that the excited carriers have two channels to relax which means that we introduced two different decay times, τ_1 and τ_2 (see [5], page 50). We find a FWHM of $12\text{ ps} \pm 1\text{ ps}$ which gives the temporal resolution of the pTRCL setup.

2.3.3 Alternative Detection Line

The above described detection line is a commercially available standard solution, which has the advantage of being rather easy to use and calibrate. However, we encountered problems with the signal to noise ratio when we wanted to detect signal in deep UV ($5.77\text{ eV} = 215\text{ nm}$) for example from boron-nitride crystals.

Actually, the system described above is disadvantageous from several points of view: the image of the sample is formed three times before arriving on the streak cathode where the detection takes place. This might introduce significant signal loss when numerical apertures of the optics are not perfectly matched. Even with UV optimized optics (mirrors and fused silica lenses) there is a 4% loss for every reflection and the streak objective has a typical transmission factor of $T = 0.50$ at 233 nm .

For these reasons the detection line depicted in figure 2.10 minimizing the number of optical components was designed and mounted. In the case where CL images are not to be measured (like in the case of boron nitrides), we can avoid to mount the PM. To record CL images, a PM could easily be introduced by mounting a retractable mirror ("flip-flop") between the UV objective and the streak camera to deviated the signal on a vertical slit with the PM behind. The grating (600 grooves/mm blazed at 300 nm for the 1st diffraction order) is mounted directly in the collimated signal beam on a rotative stage (angles can be adjusted with a precision of one second) with

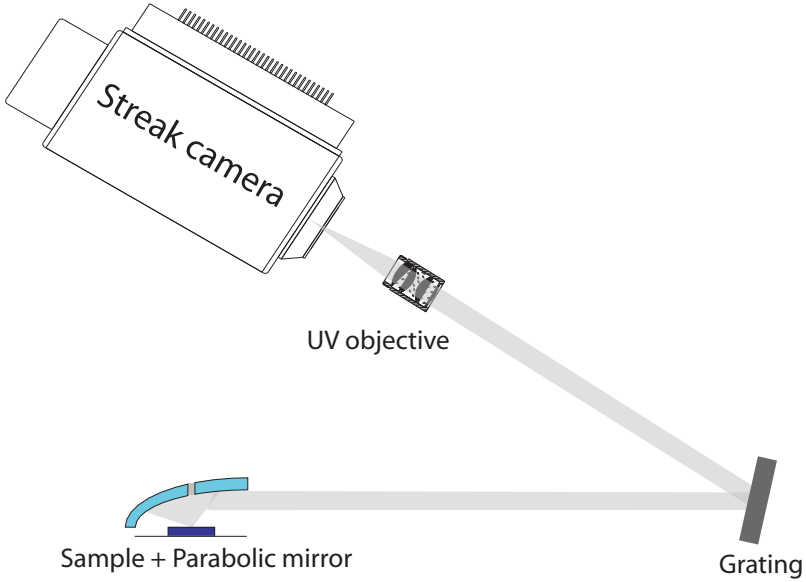


Figure 2.10: Alternative detection line minimizing the number of optical components.

two translation stages and a tilt adjustment. Translation stages are needed to align the axes of the rotative stage with the optical and the grating axes. Tilt adjustments are used to position the grating grooves perpendicularly to the optical table ("rocking" adjustment). The UV objective (OUV 430, B. Halle Optik Nachfl.) is mounted at 45 cm distance from the grating under an angle of 36.2° , determined by geometrical restrictions. The photocathode of the streak camera is directly mounted in the focal plane of the UV objective.

Alignment of the UV objective and the Streak camera is achieved with help of a HeNe Laser using the 0th order diffracted beam from the grating. The central wavelength λ is chosen by setting the corresponding angle, ϕ , on the rotative stage. The angles are calculated by means of the grating formula

(see for example [15]):

$$m\lambda = \frac{2}{N} \cos K \sin \phi \quad (2.1)$$

where $N = 600 \text{ grooves/mm}$, λ is the wavelength, m is the diffraction order (we work with $m = 1$) and $2K = 36.2^\circ$ is the angle between the optical output axes and the UV objective axes.

Since this setup doesn't include any slit the signal spot size on the Streak camera should be as small as possible to obtain sufficient spectral and temporal resolutions. The minimal spot size we were able to observe on the Streak camera CCD had a FWHM of $54 \mu\text{m}$. Applying a simplified Rayleigh criteria stating that two spots can be separated if the distance between their centers is bigger or equal to their radius and taking into account the geometry of the detection line, we find a maximal spectral resolution of 15 meV (corresponds to approximately 0.55 nm) at 5.77 eV (215 nm). The spot doubles in size towards the borders of the Streak camera photocathode (off-axis) which yields a spectral resolution of 30 meV (corresponds to approximately 1 nm). This is still good enough compared to the energy distance between the luminescence peaks we want to observe in the case of boron nitride samples. Maximal theoretical resolution of our system is given by the resolving power

$$R = \frac{E}{\delta E}, \quad (2.2)$$

where δE is the limit of resolution, i.e. the difference in energy between two lines of equal intensity that can be distinguished. The resolving power for a diffraction grating is given by $R = mN$ where m is the diffraction order (here $m = 1$) and N is the total number of grooves illuminated on the grating. The maximal diameter d of the spot on the grating is given by the dimensions of the parabolic mirror to collect CL signal and is equal to $d = 26 \text{ mm}$. We use a grating with 600 grooves/mm which yields $R = 600 \times 26 = 15600$. The theoretical maximal spectral resolution is given by 0.4 meV at 5.77 eV (corresponds to 0.01 nm at 215 nm). The above estimated experimental resolution is far above the theoretical resolution given by the resolving power of the grating.

As far as time resolution is concerned, the spot is slightly more elongated

in the temporal direction. We consider that the resolution is given by half the spot size. Application of this criteria yields a temporal resolution of 8 ps which is still shorter than the exciting pulse length. The theoretical maximum temporal resolution is given by the delay generated at the grating. This delay is given by $\delta t = \frac{R \times \lambda}{c}$, where λ is the wavelength we measure at and c the speed of light in air. Taking $\lambda = 215\text{ nm}$ we find $\delta t = 11\text{ ps}$. The overall temporal resolution of the system is thus limited by the electron pulse length and not by this new alternative detection line.

3 Bulk GaN and InGaN based Quantum Wells

3.1 Properties of the III-Nitride materials

3.1.1 Structural properties

Crystalline properties

III-nitrides are direct-band gap semiconductors that usually crystallize in a wurtzite structure. The zincblende, or cubic phase, is metastable and somewhat less common. Even so, zincblende nitrides can be epitaxially stabilized by growing on cubic substrates, such as GaAs, 3C-SiC, Si, and MgO, all oriented in the [100] direction. The atomic arrangement in the nitride crystal structures is formed by hexagonal double layers, one consisting of nitrogen and the other of metallic group-III element atoms. Each atom (group-III and N atom) is bound by four sp^3 -hybridized atomic orbitals to its nearest neighbour, which results in a tetrahedral 4-fold coordination. The two most common phases, the hexagonal wurtzite and the cubic zincblende, differ only in the stacking order of the layers. While the cubic phase results from a periodic ...ABCABC... sequence of (111) planes along the [111] direction, the wurtzite structure is formed by ...ABAB... stacks of (0001) planes along the [0001] direction, as shown in figure 3.1. This is why at the sites where a change of stacking sequence occurs (stacking faults) inclusions of cubic material may appear in a wurtzite layer.

The main difference between the two crystal structures (wurtzite and zincblende) lies in the spatial arrangement of the interatomic bonds of the atoms of the two neighboring stacks (dashed line square in fig 3.1). In the zincblende structure the second neighbors of the two central atoms have inverted positions (3.2 (a)), while in the wurtzite structure they occupy symmetric positions (3.2 (b)).

The zinc-blende unit cell can be represented by two face-centered cubic (fcc)

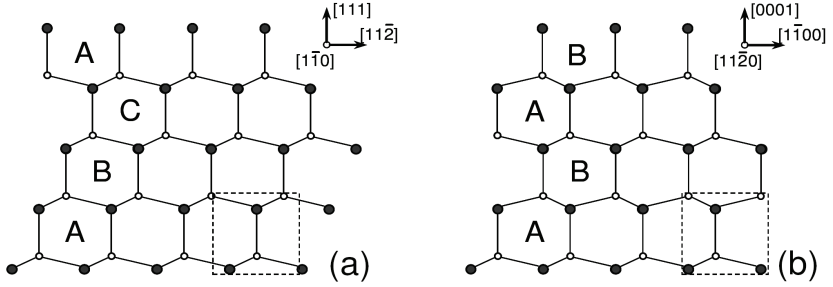


Figure 3.1: Atomic arrangement in (a) cubic zincblende and (b) hexagonal wurtzite lattice.

cells, displaced along the cell diagonal $1/4$ of its length. In wurtzite, the unit cell is represented by two interconnected hexagonal close-packed (hcp) sublattices shifted $5/8$ of lattice parameter c along the c -axis (direction $[0001]$). The most important GaN crystal planes are the c -plane (0001) , which is the most common growth plane. The most relevant structural and optical parameters of wurtzite binary nitrides are listed in table 3.1.1.

at 300 K	AlN	GaN	InN
lattice constant a_0 [nm]	0.3112	0.3189	0.3545
lattice constant c_0 [nm]	0.4982	0.5185	0.5703
bandgap E_g [eV]	6.2	3.4	1.9/0.7

Table 3.1: Crystal and band structure parameters for wurtzite nitride binaries[16].

Mechanical properties

Strain is commonly generated in layers grown on substrates with different in-plane lattice parameters, where the lattice constant of the grown layer accommodates to that of the substrate. As a result, the unit cell is deformed (bond length and angle) and strain energy builds up in the layer during growth as a function of thickness. There are two types of deformation that

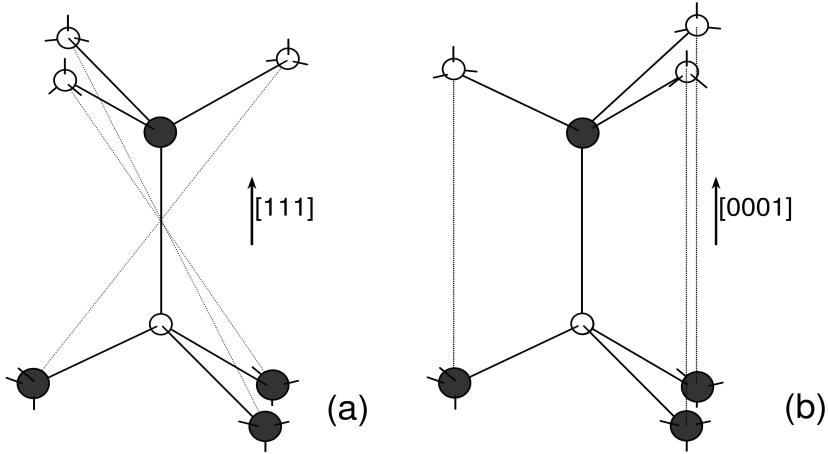


Figure 3.2: Interatomic bonds in (a) cubic zincblende and (b) hexagonal wurtzite lattice.

induce two different types of built-in strain. Biaxial compressive strain appears in the case where the in-plane lattice parameter of the substrate is smaller than that of the epilayer (3.3(a)). In the opposite case, the lattice parameter of the grown layer undergoes a biaxial tensile strain (3.3(b)). The schematic diagram in figure 3.3 represents an ideal case in which the lattice constant of the epilayer fully accommodates to the corresponding substrate. Actually, the accumulated strain energy may be released, either partially or almost completely, through the formation of structural defects (dislocations), which are very common in nitrides. This issue will be discussed in more detail in another section of this chapter.

The relation between stress, ϵ_i , and deformation, σ_i , is given by Hook's law, which takes the following tensor form for a hexagonal crystal ([17], page

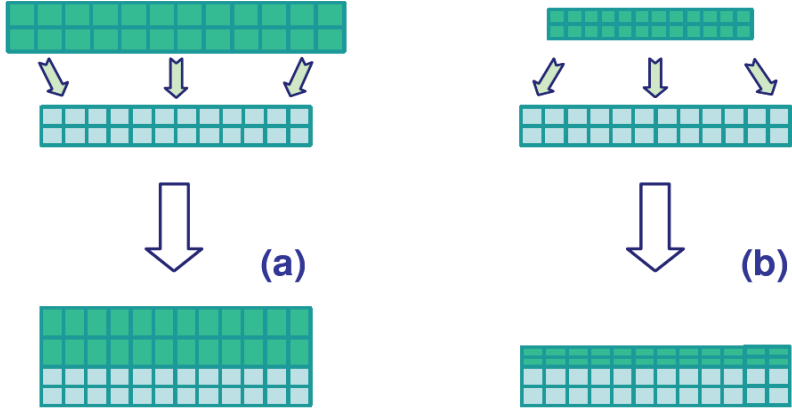


Figure 3.3: Schematic diagram of an epilayer accommodation on a substrate with different lattice parameters resulting in: (a) biaxial compressive strain, or (b) tensile biaxial strain.

141):

$$\begin{pmatrix} \sigma_1 \\ \sigma_2 \\ \sigma_3 \\ \sigma_4 \\ \sigma_5 \\ \sigma_6 \end{pmatrix} = \begin{pmatrix} C_{11} & C_{12} & C_{13} & 0 & 0 & 0 \\ C_{12} & C_{11} & C_{13} & 0 & 0 & 0 \\ C_{13} & C_{13} & C_{33} & 0 & 0 & 0 \\ 0 & 0 & 0 & C_{11} & 0 & 0 \\ 0 & 0 & 0 & 0 & C_{44} & 0 \\ 0 & 0 & 0 & 0 & 0 & \frac{C_{11}-C_{12}}{2} \end{pmatrix} \begin{pmatrix} \epsilon_1 \\ \epsilon_2 \\ \epsilon_3 \\ \epsilon_4 \\ \epsilon_5 \\ \epsilon_6 \end{pmatrix} \quad (3.1)$$

where C_{ij} are the elastic constants given in table 3.2. Due to the hexagonal crystal symmetry there are only five independent elastic constants (see [17], pages 136-139). In a planar structure where the z axis is oriented along the growth direction, the boundary conditions are such that the structure undergoes zero stress in the z direction, zero shear stresses and strains, and it has in plane symmetry of x and y directions (xyz build an orthogonal coordinate system). Consequently, $\sigma_1 = \sigma_2$, $\epsilon_1 = \epsilon_2 = \epsilon$, $\epsilon_4 = \epsilon_5 = \epsilon_6 = 0$ and $\sigma_3 = 0$. The last consequence indicates that there is no strain in the

growth direction which leads to the following relation between ϵ_3 and ϵ :

$$\epsilon_3 = -2 \frac{C_{13}}{C_{33}} \epsilon \quad (3.2)$$

The strain state of the system is characterized by only two stresses, ϵ and ϵ_3 , which are given by

$$\epsilon = \frac{a-a_0}{a_0} = \frac{b-b_0}{b_0} \quad \text{and} \quad \epsilon_3 = \frac{c-c_0}{c_0}$$

where a_0 and c_0 are the lattice constants of the unstrained crystal, and a and b those corresponding to the strained layer.

We will see in the next section that in addition to a spontaneous polarization field a piezoelectric field is induced as a result of stress. The polarization fields are at the origin of electric fields which also induce strain on the crystal via the converse piezoelectric effect [18]. However, the effect of the converse piezoelectric effect is shown to influence the final value of the internal field by less than 2% which is far above the experimental precision which justifies that it is not treated here.

Spontaneous Polarization and Piezoelectric Polarization

The wurtzite crystal structure has the highest symmetry compatible with spontaneous polarization, whose origin lies in the strong ionic component of the Ga-N bonds in the c-direction ([0001], growth direction for our samples). In addition to the spontaneous polarization which is a material property we usually have to take into account piezoelectric components induced by strain due to either lattice or thermal mismatch between the substrate and the layer. Piezoelectric fields are oriented in the c-polar (growth) direction. The piezoelectric polarization is defined in the following way (see for example [19]):

$$P_i = e_{ij} \epsilon_j \quad \text{with } i = 1, 2, 3; j = 1, \dots, 6 \quad (3.3)$$

where e_{ij} are the piezoelectric constants (for numerical values see table 3.2). Due to the crystal symmetry the number of independent piezoelectric constants is three [17]. The piezoelectric polarization in the growth direction is

		GaN	InN
Spontaneous polarization	$P_{SP}[C/m^2]$	-0.034	-0.042
Piezoelectric constants	$e_{13}[C/m^2]$	-0.35	-0.57
	$e_{33}[C/m^2]$	1.27	0.97
elastic constants	$C_{11}[GPa]$	390	223
	$C_{12}[GPa]$	145	115
	$C_{13}[GPa]$	106	92
static dielectric constants	ϵ_{11}	9.5	13.5
	ϵ_{33}	10.4	14.4

Table 3.2: Spontaneous polarization, piezoelectric, elastic and dielectric constants for wurtzite group III-nitrides. The values are taken from [16, 20]. The elastic and piezoelectric constants for GaN are experimental values corroborated by theoretical calculations. The rest of the parameters were obtained, so far, theoretically. The values of the predicted spontaneous polarization fields in III-nitrides are 5 to 20 times larger than those for arsenides.

given by:

$$P_{PZ} = e_{33}\epsilon_3 + 2e_{31}\epsilon = 2 \left(e_{31} - e_{33} \frac{C_{13}}{C_{33}} \right) \epsilon \quad (3.4)$$

The values of the spontaneous and the piezoelectric polarizations, and the elastic and dielectric constants for the binary nitrides *GaN* and *InN* (Wurtzite) are listed in table 3.2.

The total polarization is the vectorial sum of the spontaneous and the piezoelectric contribution. Discontinuities of the polarization vector at interfaces lead to charge accumulation, which in turn generates internal electrical fields. The internal electric fields typically reach values of several *MV/cm* in nitride based heterostructures [21]. Such large fields have huge influence on the optical properties of the structure. The most obvious one is the Quantum Confined Stark Effect (QCSE) which will be analyzed below since it introduces a red shift in the emission energy of quantum wells (QW) [22, 23].

3.1.2 Band structure

Wurtzite III-nitrides are wide bandgap semiconductors characterized by a bandgap structure with the valence band maximum (VB) and the conduction band minimum (CB) located at the center of the Brillouin zone (Γ , where $\mathbf{k} = 0$). III-nitrides have a direct bandgap and strong light emission efficiency at room temperature. These facts, together with the wide spectral range covered by the whole series of possible alloys, are the major advantages of III-nitrides in the field of optoelectronic devices. The band structure

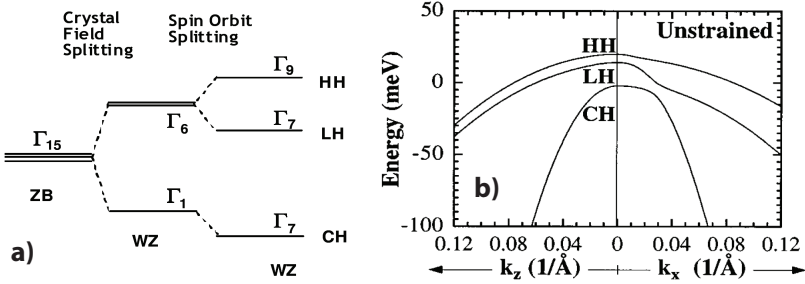


Figure 3.4: (a) Schematic illustration of the spin-orbit and crystal-field splitting in the valence band of the wurtzite nitrides (figure taken from [16]) and (b) schematic diagram of the valence band structure of wurtzite GaN near the Γ point with the heavy-hole (HH), light-hole (LH), and crystal-hole (CH) valence sub-bands (figure taken from [24]).

of wurtzite III-nitrides, unlike other direct bandgap zinc-blende III-V semiconductors, has a non-degenerate VB edge. The hexagonal symmetry of the wurtzite structure indeed induces a crystal field splitting (Δ_{CR}) of the VB into one non-degenerate Γ_1 and a two-fold Γ_6 branches. Their ordering is determined by the internal parameter u_0 (bond length) and the ratio of lattice constants c_0/a_0 (crystal ideality). Additionally, the spin-orbit splitting (Δ_{SO}) lifts the degeneracy of the two-fold Γ_6 states into non-degenerate heavy hole (HH) and light hole (LH) states, further modifying the energy of the crystal-field split-off (CH) holes. A typical VB diagram for hexagonal GaN is illustrated in figure 3.4. The energies of the valence sub-bands HH (Γ_9), LH (Γ_7) and CH (Γ_7) are given by Chuang and Chang [25] using a the-

oretical model based on the finite difference method and the effective-mass theory.

III-nitrides with hexagonal structure present different energy band profiles for the in-plane directions ($x - y$), that give different values for the effective mass m_{\parallel} (parallel to the growth plane), and for the z direction (c-axis), m_{\perp} (see for example [16] for numerical values).

Optical properties will be discussed in more detailed way in the next section dealing with InGaN based quantum wells. Excitons in III-nitrides have very large binding energies, $E_b = 26 \text{ meV}$ for GaN [26]. According to the three non degenerate valence band maximum there are three types of free excitons, A, B, and C. Their energies are given in reference [27] as 3.477 eV , 3.482 eV , and 3.499 eV , respectively.

3.1.3 Dislocations

Extended defects usually generate during the heteroepitaxial growth (because of the differences in lattice parameters between the substrate and the growing layer), or upon the growth end (during the cooling because of the difference in expansion coefficients of the two materials) allowing to reduce the accumulated strain energy. Differences in lattice parameters or thermal expansion coefficients between the nitride layer and the substrate (sapphire, SiC or Si) are the key factors to account for the strain build up in the layer. Growth conditions, substrate preparation, and the use of buffer layers will also determine whether this strain will relax and how much, thus determining the density of extended defects in the layer. Dislocation densities in GaN range from 10^{10} cm^{-2} in standard layers, down to 10^6 cm^{-2} in optimized layers thicker than 1 mm grown either using sophisticated buffer layers, or by epitaxial lateral overgrowth (ELOG).

Since dislocations are believed to be non radiative recombination centers the high luminescence efficiency of GaN and of GaN based heterostructures in particular has been an important puzzle. Understanding recombination dynamics around dislocations is a key issue for explaining luminescence properties of these structures which is one of the key subjects of this thesis work.

Dislocations are linear defects that can be defined as a shift of lattice planes due to the introduction of an additional plane. The distortion of the crys-

tal lattice is therefore located in the vicinity of the dislocation line, which traces the dislocation propagation through the crystal. The dislocation is characterized by two parameters:

1. **the dislocation line**, which separates the unaffected part of the crystal from the shifted region. It represents the line of propagation of the dislocation.
2. **The Burgers vector, \mathbf{b}** , defined as the vectorial difference between two closed lattice circuits: one in the deformed crystal that surrounds the dislocation line, and a similar one in the crystal without deformation. It is invariable around all points of a given dislocation and independent on the chosen closed circuit. Its module carries information about the shift magnitude and the strain energy released by the formation of the dislocation.

The angle between the dislocation line and its Burgers vector, α , determines the following dislocation types:

1. **Edge dislocation** with a Burgers vector perpendicular to the dislocation line ($\alpha = 90^\circ$).

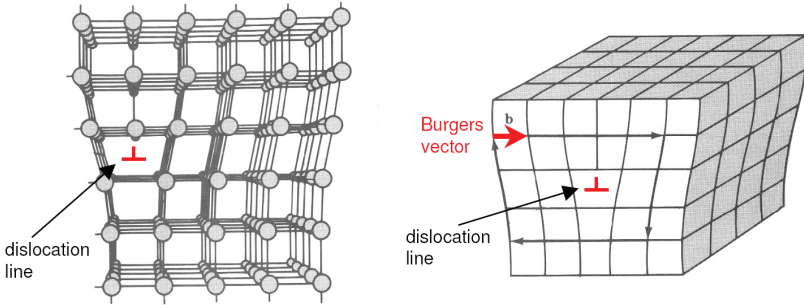


Figure 3.5: Dislocation line and Burgers vector for an edge dislocation.

2. **Screw dislocation**, with a Burgers vector parallel to the dislocation line ($\alpha = 0^\circ$).

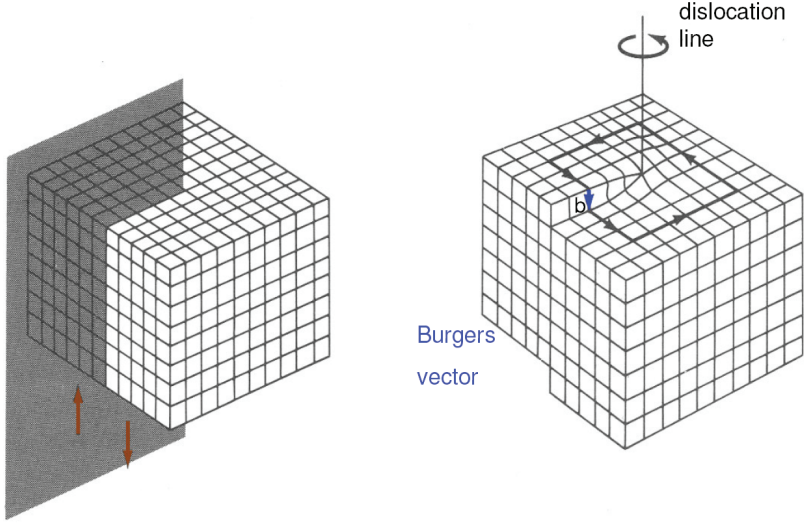


Figure 3.6: Dislocation line and Burgers vector in a screw dislocation.

3. Mixed dislocation, a combination of the two previous dislocations, having an intermediate angle between the line and the Burgers vector ($0^\circ < \alpha < 90^\circ$).

In heteroepitaxial GaN layers, either grown by MBE or MOVPE, the most common dislocation is the so called threading dislocation (TD). Generated at the interface with the substrate, they are usually parallel to the $[0001]$ direction, and propagate upwards ending, in most cases, at the layer surface. pTRCL, CL and Atomic Force Microscopy (AFM), the experimental techniques used in this thesis, allow detection of threading dislocations (TD) at the sample surface since TDs influence the luminescence properties on the surface as well as the surface texture.

TDs can be of edge, screw or mixed type and are characterized by a particular Burgers vector:

1. **pure edge a-dislocations**, with Burgers vector $b = \frac{1}{3}\langle 11 - 20 \rangle$, are

most frequent in epilayers thicker than $1\text{ }\mu\text{m}$ with a density that remains constant with the increasing layer thickness. Formed at the early stages of the growth, they are typically found in the planes of the initial hexagonal prisms, with the dislocation line parallel to the growth direction (0001).

2. **pure screw c-dislocations**, which, just as the edge dislocations, are found in the (1-100) planes, with coinciding dislocation line and Burgers vector $b = \langle 0001 \rangle$, are not that common in GaN, since they mostly interact with edge dislocations giving rise to mixed type dislocations.
3. **mixed type a+c-dislocations**, with Burgers vector $\frac{1}{3}\langle 11-23 \rangle$, are the result of the interaction between the previous two types of threading dislocations, being predominant in GaN layers thinner than $1\text{ }\mu\text{m}$.

Both edge and screw TDs nucleate in the early stages of the growth and they thread to the surface of the crystallites. Therefore, they are believed to arise from the collisions (merging) of islands during growth.

When an epitaxial layer accumulates elastic energy (as it is the case of heteroepitaxial III-nitrides), partial relaxation may occur through dislocation generation. Then, the inhomogeneous strain field distribution around the dislocation may lead to surface roughening because of induced changes in the growth regime.

3.2 Luminescence Lifetime measurement in the vicinity of TDs on GaN

In this section, we will first expose CL results and a simple model to calculate CL contrast around TDs. The fitting procedure yields the excited carrier diffusion distance L_{diff} . Then we expose local excited carriers lifetime studies on and far away from TDs. Finally, we calculate an excited carrier diffusion coefficient and find that it is in good agreement with literature.

By combining CL and AFM techniques [28], TEM and TEM CL techniques [29], CL and PL techniques [30] and combined CL, SEM and TEM techniques [31] TDs in bulk-like GaN samples have been shown to be non radiative re-

combination centers.

The main advantage of the pTRCL setup compared to the methods cited above is that it allows for direct measurements of the local effective lifetime τ . The absolute values of the radiative and non radiative lifetimes can not be determined directly. However, we get direct information about changes in these lifetimes by comparing time resolved spectra from different excitation points. To be comparable, time resolved spectra must be obtained under the same excitation condition, i.e. the excited carrier density must stay the same or vary in a controlled way. For our measurements this implies a constant or controlled probe current and a constant or controlled acceleration voltage. Under the same excitation conditions, the variations of the maximum signal of a time resolved spectrum gives information about changes in the radiative lifetime. By measuring effective lifetime changes one can conclude on changes of the non radiative lifetime. The interest of the pTRCL system is that it allows to directly verify the assumptions of the model for describing luminescence contrast around a TD which is described in detail below.

Figure 3.7 depicts a typical continuous CL spectrum of a standard bulk GaN sample¹ at a temperature of 95 K. Comparison with other measurements [32] allows to identify the main peak to free exciton recombination. The authors of [32] carry out temperature dependent photoluminescence (PL) measurements on undoped, hexagonal GaN layers. They observe three near bandgap luminescence peaks which they identify with the A, B, and C exciton recombination. The main argument is that the transition energies of the three peaks follow the semiempirical Varshni law [33] describing the bandgap evolution in function of temperature. Moreover, The fitted parameters according to the Varshni law in [32] are in good agreement with other measurements [34]. We observe one excitonic peak which corresponds to a superposition of the A, B, and C free exciton luminescence.

The grey bar on figure 3.7 indicates the spectral integration range to extract the temporal traces which are shown later (figure 3.12). The high binding energy of excitons in GaN of $E_b = 26 \text{ meV}$ [35] suggests that almost all excited carriers are free excitons at a temperature of 95 K. We can estimate

¹The sample is a commercially available (LUMILOG) GaN substrate grown on sapphire by ELOG

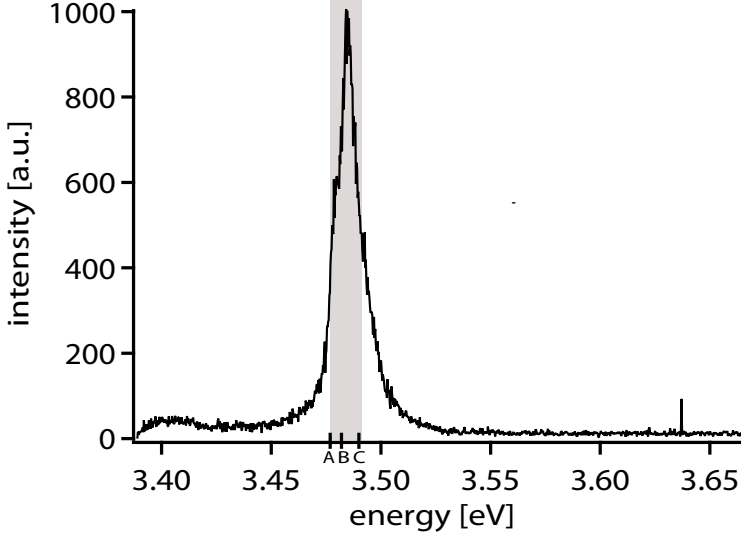


Figure 3.7: CL spectra of the GaN sample taken at a temperature of 95 K and an acceleration voltage of $V_{acc} = 8 \text{ keV}$. The grey bar indicates the integration range for time resolved spectra and the spectral bandpass for monochromatic CL images. The main peak is associated to free exciton recombination (see previous page for explanation). A, B, and C indicate the position of the A, B and C exciton peaks according to [27].

the ratio between excited carriers ρ_{ex} and excitons by means of the Saha equation [36, 37, 38]:

$$\frac{\rho_{ex}^2}{\rho_X} = \left(\frac{\mu_X k_B T}{2\pi \hbar^2} \right)^{3/2} \exp \left(\frac{-E_b}{k_B T} \right), \quad (3.5)$$

where $\frac{1}{\mu_X} = \frac{1}{m_e} + \frac{1}{m_h}$ is the exciton reduced mass in function of the electron, m_e , and hole, m_h , reduced masses (numerical values are taken from [16]). The excited carrier density is designed by $\rho_{ex} \approx 4 \times 10^{11}$ (estimated below on page 50) and ρ_X is the exciton density. We suppose that the we excite

the same number of electrons, n , and holes, p : $\rho_{ex} = n = p$. The dominating term that determines the ratio ρ_{ex}/ρ_X in equation 3.5 is given by an exponential of the ratio between the exciton binding energy E_b and $k_B T$. We find that 95% of the excited carriers should be free excitons at a temperature of 95 K. All measures presented here are carried out at 95 K and an excited carrier density $\rho_{ex} \approx 4 \times 10^{11}$. For the interpretation of the results we will thus consider the excited carriers as free excitons which also dominate the near bandgap luminescence peak.

In CL imaging, TDs on the sample surface can be seen as dark spots which makes their localization easy. In figure 3.8 a monochromatic CL image taken at the free exciton energy of a GaN bulk sample is shown. The density of dark spots on the surface is in consistency with the TD density of $4 \times 10^7 \text{ cm}^{-2}$ according to the specifications of the sample (LUMILOG). Since TDs are non radiative recombination centers their apparent diameter ($\approx 200 \text{ nm}$) in figure 3.8 should correspond to an optically active zone. Intuitively, the apparent diameter reflects the size of the electron beam excitation volume² ($d_0 \approx 400 \text{ nm}$ in diameter at an acceleration voltage of 8 kV) plus some excited carrier diffusion length L_{diff} . A simple analytical expression for excited carrier density in function of the radial distance from a dislocation can be derived following the theoretical considerations in [39]. A TD is assumed to be a radially symmetric straightline defect (parallel to the growth direction, [0001] in our sample) characterized by a radial distance r_0 within which the non radiative recombination rate is supposed to be equal to infinity (i.e. the non radiative lifetime equals zero).

We suppose that the zone $r < r_0$ is influenced by the presence of the TD and estimate r_0 from the following consideration. Electronic properties of a TD in GaN might be described by a partially filled band of electronic states in the energy gap [40]. In n-type GaN empty dislocation states are filled with electrons until the occupation limit E_{dis} reaches the fermi level E_F . Then the TD core can be treated like a negatively charged line [41, 42, 43] or in a generalized way like a negatively charged space charge zone [40]. The electronic charge distribution has been determined experimentally by J. Cai and F. A. Ponce [41] by electron holography. The authors studied edge, screw,

²Simulation with the free available CASINO software which makes use of a MonteCarlo method to trace the electron paths.

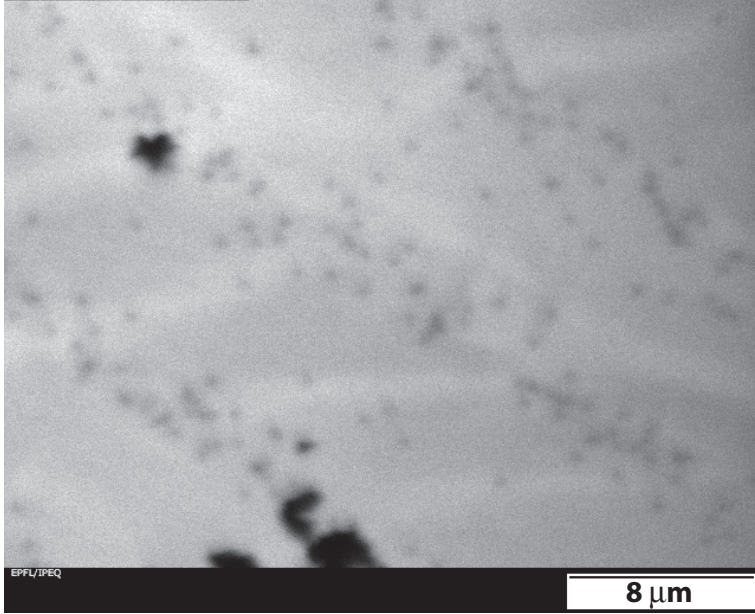


Figure 3.8: Monochromatic CL image taken at the free exciton energy ($\approx 3.48 \text{ eV}$) of a bulk-like GaN sample. The TDs can be identified as dark spots. The following parameters are used: acceleration voltage $V_{acc} = 8 \text{ kV}$ and temperature $T = 95 \text{ K}$.

and mixed dislocations in undoped GaN layers³ (similar to our samples) and found line charge densities of ≈ 0.3 , ≈ 1.0 , and $\approx 0.6 e_0/c_0$, respectively. Electrons in the vicinity of the dislocations are trapped at the dislocations. This creates a distribution of positive charges in the vicinity of the dislocation core which screen the negative charges on the dislocation core. The largest depletion length, approximately $L_{depl} = 200 \text{ nm}$, is found for screw dislocations [41]. To get an estimate of the order of magnitude of r_0 , we tentatively assume r_0 to be equal to L_{depl} . The charge accumulation at the dislocation core leads to a potential drop (see figure 3.9) of approximately

³the authors study metal organic vapor deposition grown n-type sample with a free carrier concentration of $5 \times 10^{16} \text{ cm}^{-3}$

$V_{drop} = 1.5 \text{ V}$ (see [41]) over L_{depl} which would result in an electric field of $E_{dis} \approx 0.1 \text{ MV cm}^{-1}$. Excited electrons and holes are separated by E_{dis} over a distance of L_{depl} . Furthermore, since $L_{depl} \approx 200 \text{ nm}$ there is no overlap between the electron and the hole wavefunctions anymore, thus one would expect an infinite radiative lifetime τ_{rad} . This issue will be discussed in more detail below.

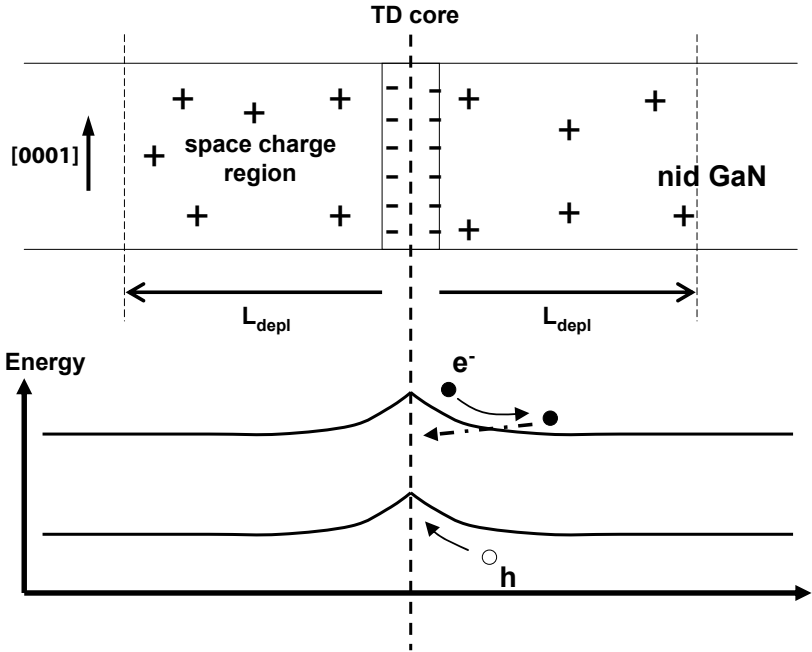


Figure 3.9: The upper part of the figure shows an illustration of a negatively charged TD with its depletion region. The lower part shows the valence band (VB) and conduction band (CB) bending around a TD and illustrates the separation of excited electron and holes near a TD. The dotted arrow illustrates the idea of electron tunneling.

To be separated by an electric field the potential difference between the electron and the hole must be larger than their binding energy. Taking the initial electron-hole separation as equal to the exciton bohr radius, $r_b \approx 3 \text{ nm}$, and E_{dis} estimated above, we find a potential difference between the electron and the hole of $V_{diff} = 30 \text{ meV}$ inside the TD depletion region. Since V_{diff} is bigger than the binding energy $E_b = 26 \text{ meV}$, the exciton is dissociated near a TD.

Outside this cylinder, $r > r_0$, the material is characterized by an effective lifetime τ . Assuming a uniform steady-state generation of carriers and no charging yields the following equation for $n(r)$, the number of excited carriers in function of the radial distance r :

$$0 = D \frac{1}{r} \frac{\partial}{\partial r} \left(r \frac{\partial n(r)}{\partial r} \right) - \frac{n(r)}{\tau} + G, \quad (3.6)$$

where G is the excited carrier generation rate, τ the effective lifetime (or measured lifetime) given by the radiative lifetime, τ_{rad} , and the non radiative lifetime, τ_{nr} , through $\frac{1}{\tau} = \frac{1}{\tau_{nr}} + \frac{1}{\tau_{rad}}$ and D is the excited carrier diffusion coefficient. The analytical solution of equation 3.6 can be written [39, 44] using the zero-order modified Bessel function $K_0(r/L_{diff})$.

$$n(r) = \begin{cases} G\tau \left(1 - \frac{K_0(r/L_{diff})}{K_0(r_0/L_{diff})} \right) & \text{for } r > r_0 \\ 0 & \text{for } r \leq r_0 \end{cases} \quad (3.7)$$

It is important to notice that $n(r)$ is a linear function of the generation rate G . This signifies that the difference between pulsed and continuous excitation lies in the value of G and does not influence the contrast profile around a TD. The use of the above model for pulsed excitation is justified if our approximations are valid.

Far away from the TD, $r \gg r_0$, an approximation to equation 3.7 can be found to be [28]: $n(r) = G\tau \left(1 - \exp\left(\frac{-r}{L_{diff}}\right) \right)$. Thus, emitted luminescence intensity around a TD, $I(r)$ for $r > r_0$, should be given by the following expression:

$$I(r) = I_0 \left(1 - \exp\left(\frac{-r}{L_{diff}}\right) \right). \quad (3.8)$$

Fitting the contrast of twelve dislocations in figure 3.8 according to equation 3.8 yields diffusion distances from $L_{diff} = 120 \text{ nm}$ up to $L_{diff} = 470 \text{ nm}$. The huge uncertainty is due to the low signal to noise ratio (see figure 3.10)

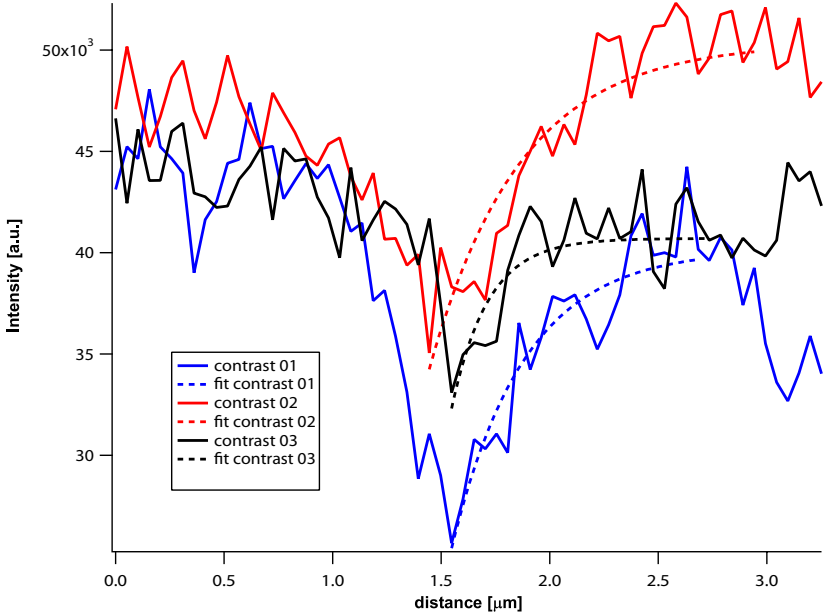


Figure 3.10: Typical CL intensity profiles extracted from figure 3.8. Thick lines correspond to the measured data and dotted lines to fits according to equation 3.8. Fits to Contrast 01 to 03 yield $L_{diff} = 340 \text{ nm} \pm 40 \text{ nm}$, $L_{diff} = 420 \text{ nm} \pm 50 \text{ nm}$ and $L_{diff} = 170 \text{ nm} \pm 50 \text{ nm}$, respectively.

of the measurement which makes the fitting difficult. Working with a higher probe current would increase the generation rate G and thus improve the signal to noise ratio. The probe current is up to now a fundamental limitation of our setup. In order to get stable working conditions, we use an average UV laser power of $\approx 100 \text{ mW}$ which corresponds to an efficiency of 10% for third-harmonic generation. Under stable conditions we generate an

average probe current of 10 pA , i.e. one electron per pulse.

Continuous CL measurements were carried out on a standard CL setup in another laboratory at EPFL. The following parameters were used: $V_{acc} = 8\text{ kV}$ and a probe current of 40 nA (more than thousand times higher than with the pTRCL setup) yields a diffusion distance of $L_{diff} = 180\text{ nm} \pm 20\text{ nm}$. Using L_{diff} and the measured bulk lifetime $\tau = 40\text{ ps}$ (see below), we can estimate a free exciton diffusion coefficient of $D_{ex} \approx 4\text{ cm}^2\text{ s}^{-1}$.

To get a better idea of the accuracy of our value of D_{ex} we want to compare it with published values. We find that our measured diffusion coefficient, $D_{ex} \approx 4\text{ cm}^2\text{ s}^{-1}$, and diffusion distance $L_{diff} = 180\text{ nm} \pm 20\text{ nm}$ fit well into the results of Mickevičius *et al.* depicted on figure 3.11 (using a lifetime of 42 ps). Mickevičius *et al.* [45] use the transient grating method to measure diffusion coefficients, D , of GaN epilayers grown under different conditions. Using Saha's equation at room temperature we still find that 47 % of the excited carriers are excitons due to their high binding energy. Thus D is a mixture between exciton and ambipolar diffusion coefficient. Figure 3.11 shows their measured diffusion coefficient and the diffusion length in function of the effective lifetime.

For the pTRCL study, the first approach was to measure luminescence lifetimes on and far away ($\approx 1\mu\text{m}$) from TDs. Our results show (see figure 3.12) up to 25 % decrease of the effective lifetime, τ , when displacing the excitation spot from a dislocation free-zone to a dislocation (42 ps down to 30 ps). One also sees a decrease of the maximum signal intensity between measurements off and on dislocation. As stated above this normally indicates an increase in radiative lifetime, τ_{rad} , equivalent to a decrease of the radiative recombination probability, $p_{rad} = 1/\tau_{rad}$. Unfortunately, the pulsed laser intensity and thus the probe current vary during the measurement. We can not safely conclude that this observed intensity variation is due to unstable experimental conditions or to an increase of τ_{rad} . The 25 % decrease of the effective lifetime is most probably due to a decrease of the non radiative lifetime indicating that non radiative recombination becomes predominant when approaching a dislocation. According to the above proposed model, the presence of a TD will influence the recombination of excited carriers in a cylinder around the TD with a diameter of approximately 200 nm . Taking into account the diameter of the excitation volume $d_0 \approx 400\text{ nm}$ at $V_{acc} = 8\text{ kV}$ and an excited carrier diffusion length of $L_{diff} \approx 180\text{ nm}$ we

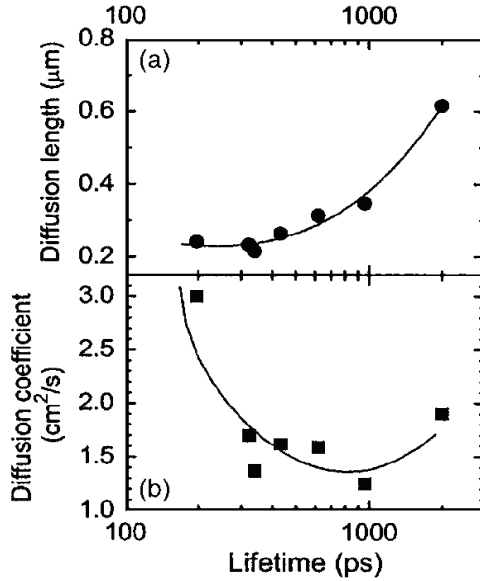


Figure 3.11: Carrier diffusion length (a) and diffusion coefficient (b) vs carrier lifetime in GaN epilayers on sapphire substrates grown under various conditions. The lines are guide to the eye. Figure taken from reference [45].

can see that only a part of the generated carriers recombines within the TD depletion region even when exciting directly on the dislocation spot. For this reason the measured lifetime on the dislocation corresponds to an average between bulk and on dislocation lifetime.

This might explain why we only observe a small variation of the radiative lifetime in figure 3.12 despite of the supposed complete separation of the electron and the hole.

The excited holes will be trapped on the TD core very rapidly and recombine non radiatively (see figure 3.9). This trapping is very fast and adds most likely a non radiative recombination channel which would explain a shorter

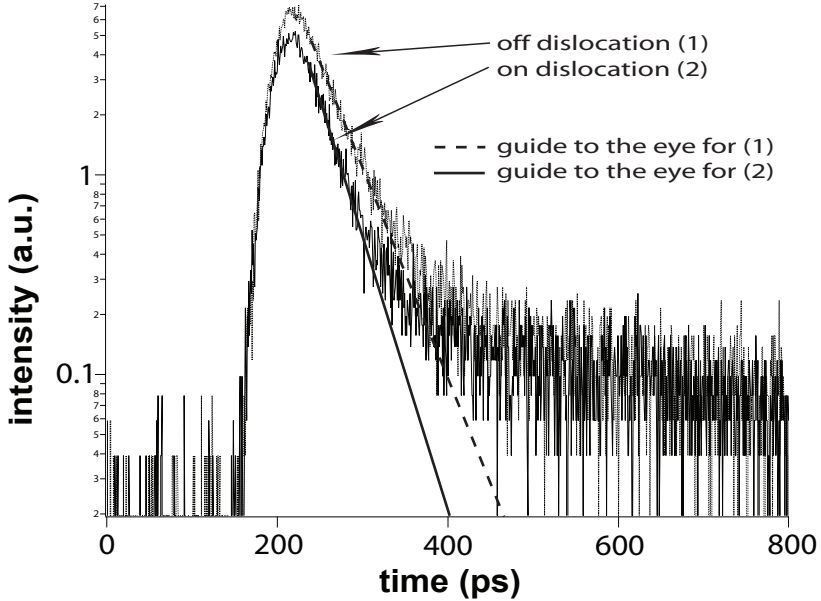


Figure 3.12: Time traces showing the decay of the free exciton obtained on bulk GaN. Traces are obtained by exciting on (2) and far from a dislocation (1). The dashed and full lines are guides to the eye. Measurement conditions are $V_{acc} = 8 \text{ kV}$ and $T = 95 \text{ K}$

non radiative recombination time on the dislocation. To establish equilibrium conditions, excited electrons will find a way to tunnel to the dislocation core (see lower part of figure 3.9). However, in such a simple model as the one introduced here this effect can not be addressed and further studies are needed.

In order to gain more accurate information about carrier lifetimes, we can try to find ways how to effectively reduce the interaction volume. Three different ways are proposed to achieve this goal:

1. To work at low acceleration voltage ($\approx 1 \text{ kV}$, see [46]) to effectively decrease the interaction volume to a few nm .

2. To use samples thin enough so that the electron beam can pass through the sample. This would reduce the interaction volume to the electron beam diameter on the sample surface, independent of the acceleration voltage.
3. To use a heterostructure (for example quantum wells) with a few nanometer thick structure at the surface exhibiting higher recombination energy than the rest of the sample. The resolution of monochromatic CL images detected at high energy will be limited only by the electron beam diameter on the sample surface plus some diffusion distance (see figure 3.13).

The first method was used by Pauc et al. [46] to determine diffusion distances of excited carriers in GaN by CL. Yamamoto et al. [29] used thin samples prepared for TEM measurements to characterize dislocations in GaN.

In parallel with the ongoing work on GaN microdisks, having thicknesses of about 100 nm, we have implemented the third method by growing an InGaN/GaN double QW structure on a GaN template. The surface well exhibits a higher energy than the well further away from the surface acting as energy barrier for the carriers generated in and below it. The results obtained on this structure will be presented in the next section.

3.3 TDs in InGaN Quantum Wells

As mentioned above, the idea here is to use heterostructured material to reach better resolution in CL mode. We chose to grow double InGaN QW on the GaN template from LUMILOG studied in the previous section. We grew first a "low energy" QW followed by a thin "high energy" QW near the surface. High and low energy refer here to the recombination energies of excitons we are looking at.

InGaN is usually a very disordered material. It is believed that InGaN alloy composition fluctuates due to In phase separation, giving rise to the formation of In-rich nanoclusters (see [47]), that may even act as quantum dots (QDs). Excitons can be localized at such QDs, no longer behaving as free

excitons. We can not distinguish between free or bound excitons in our measurement and will thus just design the excited carriers as excitons.

The QW energy is changed by choosing different well thicknesses (3 nm for the low energy QW and 1.5 nm for the high energy QW). The larger part of the primary electron interaction volume at $V_{acc} = 8 \text{ kV}$ is located beneath the low energy QW. Excited carriers beneath the low energy quantum well will recombine after diffusion either in the template or they will be captured by the low energy well [48]. Excited carriers are prevented from diffusing into the high energy well which would worsen the CL resolution. Figure 3.13 illustrates the idea of a "barrier well". Spatial resolution of monochromatic CL maps from the high energy well should be given in such a configuration by the probe beam diameter on the sample surface ($\approx 50 \text{ nm}$) plus some diffusion distance L_{diff} . More detail about optical properties of InGaN QWs will be given below. The huge piezoelectric and spontaneous polarization (in InGaN, the total polarization is to 10% spontaneous and to 90% piezoelectric) constants give rise to polarization fields in the QW which induce huge internal electrical fields [21] of several MVcm^{-1} . Such electric fields influence the optical properties of the structures and induce the Quantum Confined Stark Effect [49] (QCSE) leading to a redshift [22, 23] of the emission energies and to a separation of the electron and hole wavefunctions resulting in a decrease of the radiative lifetime. In the next section we will give an overview on how to measure and calculate the internal electric field. We will also briefly review how to calculate energy levels in an QW with internal electric fields including excitonic (i.e., coulomb attraction between electrons and holes) effects.

3.3.1 Internal Electric Field

To calculate the internal electric field \mathbf{E}_{int} we need to know the total or built in polarization, \mathbf{P} and the electrostatic displacement \mathbf{D} . In a QW, the total polarization is the sum of spontaneous and piezoelectric polarization:

$$\mathbf{P} = \mathbf{P}_{SP} + \mathbf{P}_{PZ}. \quad (3.9)$$

We can write for \mathbf{D} :

$$\mathbf{D} = \epsilon_{33}\mathbf{E}_{int} + \mathbf{P}_{PZ} + \mathbf{P}_{SP} \quad (3.10)$$

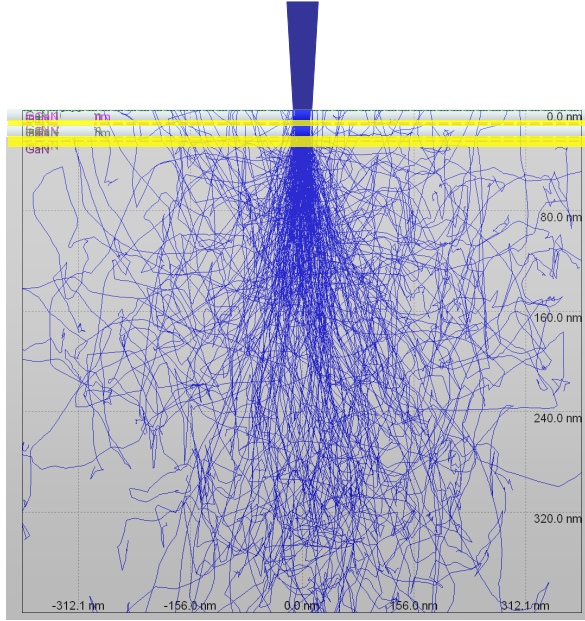


Figure 3.13: Illustration of the "barrier well" principle. A low energy QW situated below the high energy QW serves as an energetic barrier to hinder excited carriers from recombining in the high energy well. The acceleration voltage is set to 8 kV to calculate the blue electron paths.

where \mathbf{P}_{PZ} is expressed in function of strain and the piezoelectric constants through equation 3.4. Solving for \mathbf{E}_{int} yields:

$$\mathbf{E}_{int} = \frac{(\mathbf{D} - \mathbf{P}_{SP}) - \mathbf{P}_{PZ}}{\epsilon_{33}}. \quad (3.11)$$

The displacement field is determined by the free-charge distribution in the material:

$$\nabla \mathbf{D} = e(p - n) \quad (3.12)$$

with e the electron charge, and p and n the hole and electron densities, respectively. Evaluation of the electric field \mathbf{E}_{int} inside the semiconductor requires in general a self-consistent solution of equation 3.11 and equation 3.12. However, in the low free-carrier-density-limit (see discussion below) internal electrical fields can be calculated without explicitly solving the differential equation system. To calculate the internal field, we will follow the approach by Bernardini and Fiorentini [50]. As a starting point, let's consider the internal electric field in a large bulk sample. Intuitively, if a large overall internal field existed there would be a constant flow of a net charge current. This is not the case in massive samples which leads to the conclusion that the overall electric field is zero. The piezoelectric component is taken to be zero, we consider a strain free bulk sample. Therefore we deduce⁴:

$$\mathbf{D} = \mathbf{P}_{SP} \quad (3.13)$$

Let's suppose that we insert a series of layers in the massive sample. The electric field in layer j , \mathbf{E}_j is given by:

$$\mathbf{E}_j = \frac{\mathbf{D} - \mathbf{P}_j}{\epsilon_j}. \quad (3.14)$$

which becomes the following equation if equation 3.13 holds:

$$\mathbf{E}_j = \frac{\mathbf{P}_{SP} - \mathbf{P}_j}{\epsilon_j}, \quad (3.15)$$

where \mathbf{P}_j is the total polarization field in layer j . The index j runs over both barriers and QWs. \mathbf{P}_{SP} is the spontaneous polarization of the massive material which will here play the barrier role. If this massive material is also strained, \mathbf{P}_{SP} in equation 3.13 has to be replaced by $\mathbf{P}_{SP} + \mathbf{P}_{PZ}$ where \mathbf{P}_{PZ} accounts for the strain induced piezoelectric component. Since each QW is subject to the electrical field \mathbf{E}_j a potential drop of $\Delta V_j = |\mathbf{E}_j| l_j$ occurs where l_j is the thickness of the j -th layer. For equation 3.13 to hold nor one

⁴There is a polarization discontinuity at the surface when going from the sample to vacuum. This discontinuity has to be counterbalanced by a surface charge accumulation of the same magnitude than the polarization field. The electric field has a very complicated behaviour in this surface region which reaches into the sample over a distance l_c which can reach several tens of nanometers. However, at distances in excess of l_c we can safely assume $\mathbf{D} = \mathbf{P}_{SP}$.

of the V_k neither the sum over V_k must exceed the bandgap E_{gap} :

$$\sum_k l_k |\mathbf{E}_k| < E_{gap} \quad (3.16)$$

If condition 3.16 is not verified and the potential drop approaches the bandgap, the Fermi levels also approach the conduction and valence bands which leads to important charge accumulations [51] on the opposite sides of the sample and equation 3.13 holds no longer. This can happen for thick layers. The measured (see below) internal field of the thin InGaN QW ($l = 1.5 \text{ nm}$) is $E_{int} = 1.8 \text{ MV/cm}$. The critical thickness l_c is given by $l_c = E_{gap}/E_{int} \approx 10 \mu\text{m}$ which is much larger than the overall thickness of the structure we study. A convenient approximation to condition 3.16 consists in applying periodic boundary conditions:

$$\sum_k l_k \mathbf{E}_k = 0, \quad (3.17)$$

where k runs over all layers. Condition 3.17 signifies that the displacement field is determined subjected to the condition of zero average electric field in the QW structure.

Introducing equation 3.14 into equation 3.17 yields the displacement field \mathbf{D} . Reinsertion into equation 3.14 gives a simple expression for the electric fields in the wells and barriers:

$$\mathbf{E}_j = \frac{\sum_n l_n \mathbf{P}_n / \epsilon_n - \mathbf{P}_j \sum_n l_n / \epsilon_n}{\epsilon_j \sum_n l_n / \epsilon_n}. \quad (3.18)$$

The thicknesses of the InGaN QW we are going to study is very small (1 nm to 1.5 nm) compared to the GaN substrate on which they are grown, we suppose that the GaN remains unstrained and the InGaN adapts its lattice constant. Thus for GaN, which is the barrier material, we only have to take into account P_{SP} from table 3.2.

The spontaneous polarization for the ternary alloy $\text{In}_x\text{Ga}_{1-x}\text{N}$, where x corresponds to the In fraction, does not follow a Vegard like interpolation law taking into account the spontaneous polarizations from InN and GaN . It has been shown [52] theoretically and experimentally that the spontaneous

polarization of $In_xGa_{1-x}N$ is given by:

$$P_{SP}(x) = -0.042x - 0.034(1-x) + 0.038x(1-x). \quad (3.19)$$

The first two terms in equation 3.19 correspond to the standard linear interpolation between the binary compound, the last term is the bowing parameter describing the nonlinearity to quadratic order.

As far as the piezoelectric component is concerned, formula 3.4 is a first order approximation. To get accurate values, quadratic corrections in the stress ϵ have to be taken into account [53, 52]:

$$P_{GaN}^{PZ} = -0.918\epsilon + 9.541\epsilon^2 \quad (3.20)$$

$$P_{InN}^{PZ} = -1.373\epsilon + 7.559\epsilon^2 \quad (3.21)$$

where $\epsilon(x) = \frac{a_{sub}-a(x)}{a(x)}$ is the basal strain of the InGaN layer, $a(x)$ and a_{sub} being the lattice constants of unstrained InGaN at In composition x and of the substrate, respectively. Vegard's law can be used to calculate $a(x)$ directly as a function of In composition:

$$a(x) = 3.189 + 0.356x. \quad (3.22)$$

Contrary to the case of spontaneous polarization, Vegard's law holds [52] for the piezoelectric polarization:

$$P_{PZ}(x) = xP_{PZ,InN}[\epsilon(x)] + (1-x)P_{PZ,GaN}[\epsilon(x)] \quad (3.23)$$

Here, Vegard's law holds for the piezoelectric polarization for the ternary alloy InGaN because the quadratic corrections to the piezoelectric polarizations of the binary alloys InN and GaN are already included in P_{GaN}^{PZ} and P_{InN}^{PZ} .

3.3.2 Effects of the Internal electrical field on optical properties

As described in the previous section, one of the peculiarities of InGaN QWs lies in the presence of an electric field, whenever the growth is performed in a direction that is not perpendicular to the [0001] direction. Once the internal electric field is known, it is possible to solve the Schrödinger equation and to

determine the wave functions and the energy level position in the low density regime, meaning in a regime where the injected free carriers do not screen the electrical field.

To get an idea about whether or not the internal electrical field is screened in our sample we might use the following argument: the excited carrier surface density ρ_{ex} should be much smaller than the surface charge ρ_{pol} due to the change in polarization when crossing a surface, $\rho_{ex} \ll \rho_{pol}$. Maxwell's equations yield $|\mathbf{D}_{sample}| - |\mathbf{D}_{vacuum}| = \rho_{pol}$ for the displacement field \mathbf{D} component normal to the surface (parallel to the [0001] direction). According to the above analysis we assume $\rho_{pol} = |\mathbf{D}_{sample}| = |\mathbf{P}_{SP,GaN}| = -0.034 C/m^2 \approx 2.1 \cdot 10^{13}$ elementary charges/cm² (see table 3.2 for the numerical value of $|\mathbf{P}_{SP}|$). Since we can not exactly estimate ρ_{ex} we have to make some simplifying assumptions and try to find a maximal value:

1. We take standard work conditions for this sample: A primary electron acceleration voltage $V_{acc} = 8 kV$ and a probe current of 10 pA or 1 electron per pulse.
2. The excitation volume possesses a spherical symmetry with a radius $r = 100 nm$.
3. To create an electron-hole pair the energy three times that of the gap is needed.

We find $\rho_{ex} \approx 4 \cdot 10^{11}$ elementary charges/cm². Considering that the internal field is not screened in our experiments seems to be a reasonable assumption since $\rho_{ex} \ll \rho_{pol}$.

As already mentioned before the internal electrical field is the origin of a potential variation within the QW and the barrier in function of distance. This means that inside a QW the electrons and the holes accumulate at opposite sides and emission energies will be smaller in comparison to the field free case. This effect, causing the luminescence redshift (shift towards smaller energies), is called the Quantum-Confined Stark Effect (QCSE) and was first observed in GaAs-AlGaAs QW in 1983 by Chemla *et al.* [54]. Figure 3.14 illustrates the effect of an internal electrical field on the bandstructure in a QW and the resulting hole and electron wavefunction separation. To interpret our experimental results we will need to calculate the transition

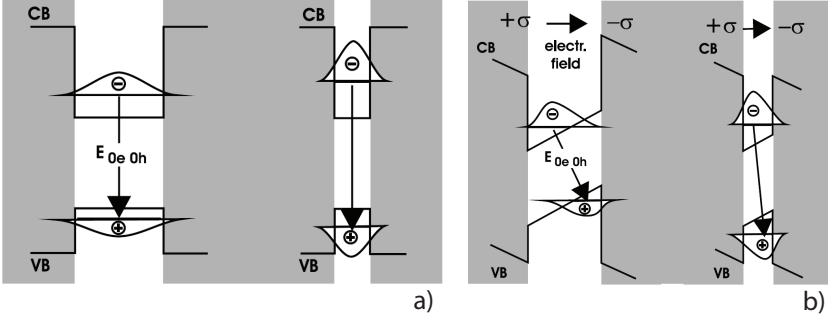


Figure 3.14: Illustration of the energy band in a QW in the field free case (a) and with an internal electrical field (b) (Illustration taken from [19]).

energy in a QW including excitonic effects and the effect of the internal electric field. We will briefly expose here the used methods. Details can be found in appendix A. The transition energy E in a QW is given by the following expression:

$$E = E_{gap} + E_e + E_h - Ry, \quad (3.24)$$

where E_{gap} is the strained fundamental bandgap of the well material (here InGaN), E_e and E_h are the confined electron and hole energies respectively, and Ry is the excitonic Rydberg term. The internal electric field influences E_e , E_h , and Ry . E_e and E_h are obtained by solving the one particle Schrödinger equation for the envelope electron and hole wave functions and taking into account the internal electric field through potential terms $V_e(z_e)$ and $V_h(z_h)$, where z_e and z_h indicate the electron and hole positions on the axes perpendicular to the growth plane. To calculate Ry we will follow the method by Leavitt and Little [1]. They derived an expression for Ry as an integral (over the coordinates of the electron and hole perpendicular to the confining layers) of a prescribed function multiplied by the squares of the electron and hole subband envelope functions. Their main approximation is based on the fact that the electron and hole distance on an axes perpendicular to the layers is larger than $0.01 r_{b,X}$ where $r_{b,X} = 2.8 nm$ is the GaN

exciton Bohr radius. Due to the separation of the electron and hole through the internal electrical field this is always the case. Numerical solution of the equation described above to calculate E and Ry is executed using a code developed by B. Damilano, N. Grandjean, and S. Dalmaso [55]. We will use this code below to calculate the exciton recombination energy in function of QW thickness and the internal electric field.

3.3.3 Sample Structure

We have studied two types of heterostructures grown by metal-organic vapor phase epitaxy (MOVPE) in an Aixtron 200/4 RF-S reactor. Sample growth was carried out at EPFL by E. Feltin in the group of Prof. N. Grandjean. Both types of samples are grown on 2 inch c-plane sapphire substrates at a temperature of 740°C . Samples (A) consist of a single $\text{In}_x\text{Ga}_{1-x}\text{N}/\text{GaN}$ QW (1.5 nm thick, $x \approx 15\%$) with or without any GaN cap layer deposited on standard 2 μm thick GaN templates with TD density of $7 \times 10^8 \text{ cm}^{-2}$.

Another sample (B) consists of two $\text{In}_x\text{Ga}_{1-x}\text{N}/\text{GaN}$ ($x \approx 15\%$) QWs grown on commercially available ELO substrate we studied in the previous section on bulk GaN. As already stated, this substrate presents a low TD density of $4 \times 10^7 \text{ cm}^{-2}$. In this sample the active structure is composed of a 3 nm InGaN/GaN QW, a 10 nm GaN barrier, a thin 1.5 nm InGaN/GaN QW and a GaN cap layer (10 nm). The structure is depicted in figure 3.15. The thinner QW is located close to the surface and its luminescence peak is at higher energy (3.10 eV) than the the luminescence peak of the second well (2.92 eV). The use of a larger well below the thin one improves the spatial resolution in CL imaging as explained before. Thus CL resolution of the surface QW is given by the electron beam diameter ($\approx 50 \text{ nm}$) plus some excited carrier diffusion distance.

3.4 Experimental Results

3.4.1 Continous CL

We will first present standard (quasi continuous) CL on Sample (B) (see schema on figure 3.15) which was used to characterize the sample before doing time resolved measurements on selected spots. CL spectra recorded at

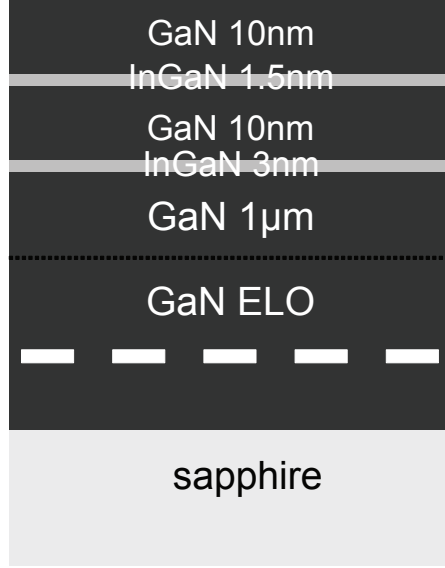


Figure 3.15: Structure of sample (B) consisting of two InGaN QWs of 1.5 nm (near the surface) and 3 nm (far from the surface).

95 K is shown in figure 3.16. Two main peaks corresponding to the emission energies of the two quantum wells are clearly distinguished. The high energy peak (thin QW) is observed at 3.10 eV and the low energy peak is centered at 2.92 eV (thick QW). We recorded monochromatic CL images at 95 K in the energy range from 2.8 eV to 3.2 eV , with a $\approx 15\text{ meV}$ step. The bandpass for CL images is typically 20 meV and we use integration times of 1 ms to 5 ms per pixel. The acquired image size is $640\text{ px} \times 480\text{ px}$ yielding acquisition times per image between $\approx 5\text{ min}$ and $\approx 25\text{ min}$. Monochromatic CL images centered on the high energy peak show a fine line structure (see figure 3.17). Contrary to our expectations, no dark spots are observed. Interestingly, we observe a perfect contrast inversion between the CL images in figure 3.17 meaning that the dark lines in figure 3.17(a) turn into bright ones in figure 3.17(b) when changing the detection energy from the low energy side of the QW emission peak to its high energy side.

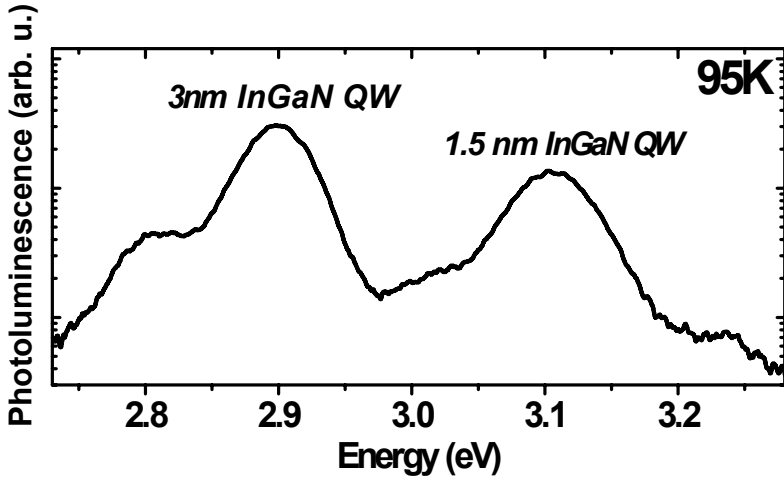


Figure 3.16: Spectra of sample (B). Taken at 95K and with an acceleration voltage of $V_{acc} = 8 \text{ kV}$. The luminescence peaks corresponding to the thin (1.5 nm) and to the thick (3 nm) QW can be seen centered at 3.10 eV and 2.92 eV respectively.

We would like to correlate the observed fine line pattern on monochromatic CL images (see 3.17) and the contrast inversion to the particular surface morphology of InGaN based QWs. The surface morphology was investigated by atomic force microscopy (AFM) measurements. Obtained results will be detailed in the next section.

3.4.2 AFM measurements

To understand the surface morphology, AFM imaging of sample A surface was carried out at different stages of the growth. A scan of the standard GaN template surface recorded before the growth of the InGaN layer is displayed in figure 3.18. The density of TD terminations, determined by the number of dark spots (pits), is about $7 \times 10^8 \text{ cm}^{-2}$. The surface morphology is smooth and characterized by numerous terraces. The terrace step height is 0.5 nm

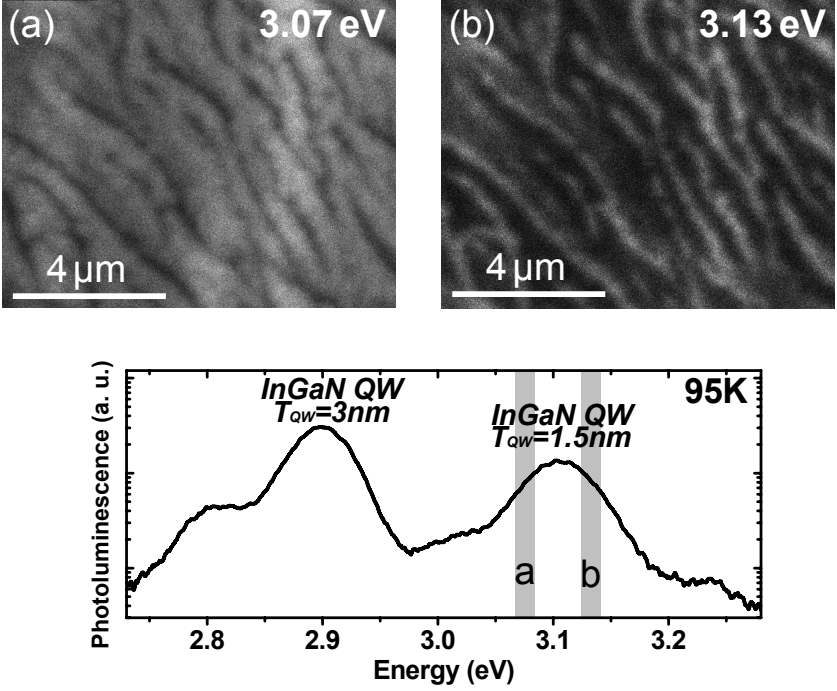


Figure 3.17: Monochromatic CL images centered at the high energy side (b), 3.13 eV, and at the low energy side (a), 3.07 eV, of the thin QW luminescence peak. Gray bars on the QW spectra indicate the detection energy. Their width on the energy scale corresponds to the energy bandpass we set on the monochromator.

on average and corresponds to a molecular bilayer thickness. The root mean square (rms) roughness is 0.25 nm for a $2 \times 2 \mu\text{m}^2$ scan area. Another point of interest is the slight misorientation of the (0001) surface measured from the AFM image. We measure $0.26 \pm 0.02^\circ$, in good agreement with the 0.25° misorientation of the sapphire substrate.

The surface morphology of the 1.5 nm thick InGaN epilayer deposited on

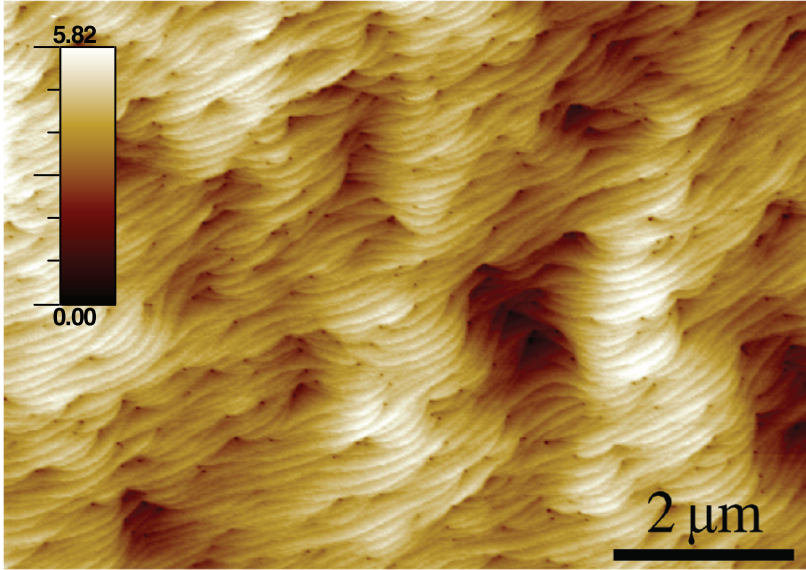


Figure 3.18: AFM image of the GaN surface before the deposition of the InGaN QW.

this surface reveals very interesting features (see figure 3.19 and inset). The first observation is the strong increase of the surface roughness (from $rms = 0.25\text{ nm}$ on the GaN substrate to $rms = 0.65\text{ nm}$ on the deposited InGaN epilayer). Actually, the surface is now characterized by deep valleys oriented in the $\langle 1 - 100 \rangle$ directions. The depth of these valleys is close to 1.5 nm , which is the nominal thickness of the InGaN epilayer. It means that, at least before the GaN capping, the well thickness is quite inhomogeneous along a direction perpendicular to the valley direction. The typical modulation length of the QW thickness is $0.3 \sim 0.5\text{ }\mu\text{m}$. Notice that the same surface feature is observed for the InGaN epilayers deposited on the ELO templates (figure 3.19 (b)) used for the measurements on bulk GaN presented in the previous section. The only difference is the modulation length which is larger for the ELO grown sample. In fact, the valley formation is closely

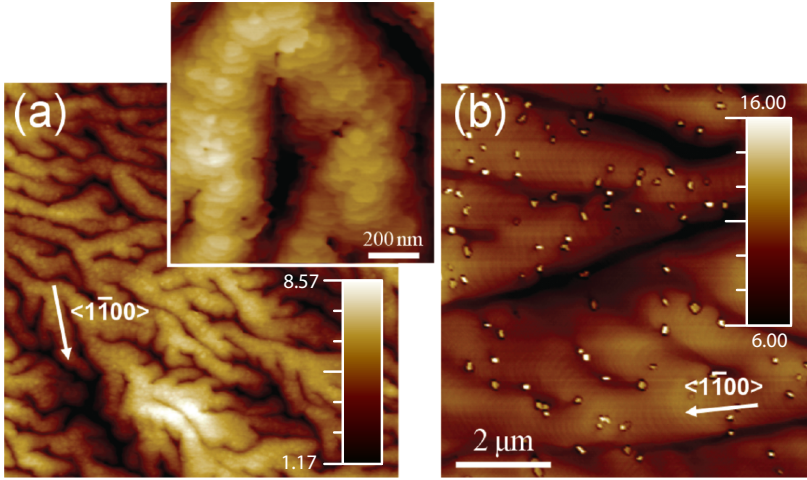


Figure 3.19: AFM image of the surface after the deposition of a 1.5 nm thick InGaN layer on a standard GaN on sapphire substrate (a) and the ELO GaN substrate (b). The inset shows a AFM image of the standard GaN on sapphire substrate at a higher magnification.

related to the presence of dislocations at the growing surface which explains the lower valley density on ELO samples. The influence of dislocations on the valley formation will be discussed hereafter in more detail.

The surface of the InGaN epilayers was too rough to allow for the observation of the dislocation terminations in the AFM images. Figure 3.20(b) shows an AFM image of the surface after the deposition of a 10 nm thick GaN cap layer. The morphology is very similar to that observed on the InGaN surface although slightly smoother after GaN deposition. Consequently, dislocation terminations are clearly visible again, which enables identifying their role on the peculiar growth mode of InGaN layers. Figure 3.20(b) is a magnification of the AFM image displayed in figure 3.20(a). We can see that dislocations hinder the InGaN step flow growth creating a surface depression behind them. This is the main difference compared to GaN for which the

dislocation terminations have weak impact on the growth mode. The reason for such difference could be related to strain.

We thus tentatively propose that valleys may be formed by the coalescence of surface depressions induced by dislocation terminations. This means that the bottoms of the valleys are populated by a significant number of dislocations. The larger modulation of the QW thickness for the ELO grown sample also supports this interpretation which was recently published by Grandjean *et al.* and our group [56].

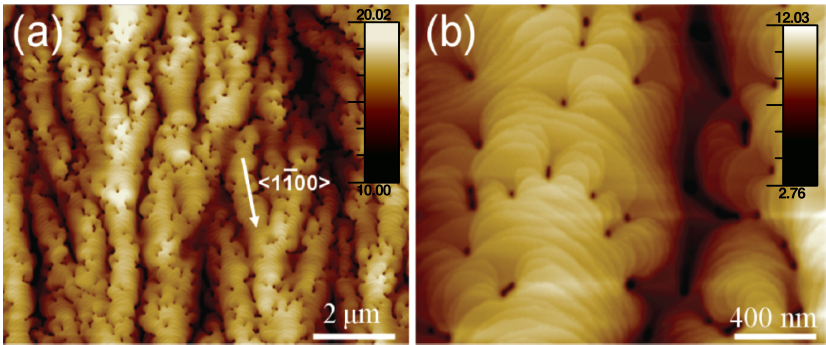


Figure 3.20: AFM image of the sample A surface after the deposition of a 10 nm thick GaN cap-layer on the InGaN QW and (b) magnification ($1 \times 1 \mu\text{m}^2$) showing the influence of the dislocation termination on the step-flow growth.

3.4.3 Correlation between CL and AFM measurements

Comparison of the fine line structure observed on monochromatic CL images (3.17) and the valley structure on AFM images (3.20 (b)) suggests that these structures coincide. Figure 3.21 (a) shows an AFM image of the sample (B) surface at the same magnification than the monochromatic CL images displayed on figure 3.21 (b) and (c). The observed contrast inversion on monochromatic CL images can be interpreted in the following way.

The QW width is very inhomogeneous. Due to quantum confinement, ex-

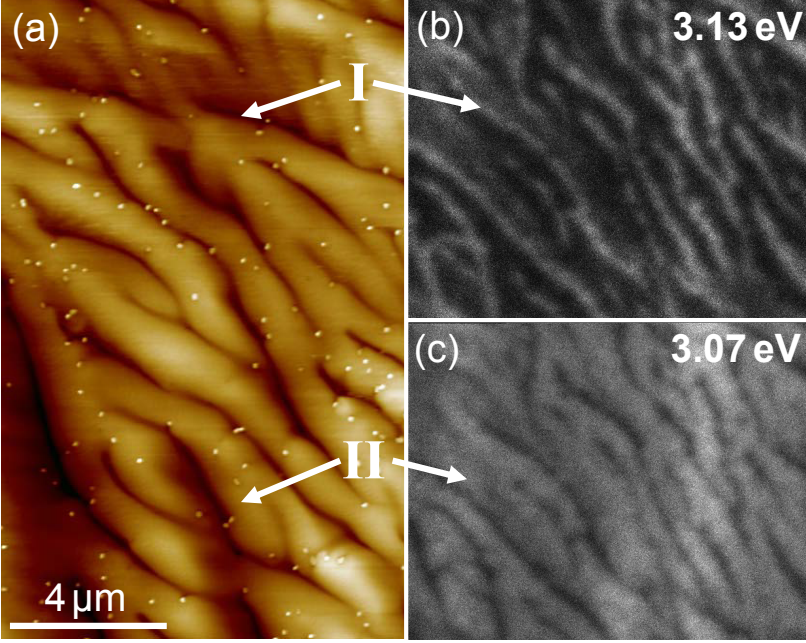


Figure 3.21: AFM image (a) of the surface of sample (B) and monochromatic CL images (different location than the AFM images) at 3.13 eV (b) and 3.07 eV (c). The CL images correspond to the high and low energy side of the thin InGa_N QW luminescence peak, respectively. I indicates a valley zone while II indicates a zone outside the valleys.

cited carriers recombine at higher energy in regions where the QW is thinner than the nominal thickness. Since the QW thickness in the valley regions is reduced, we expect higher energy emission there. This explains why the valley regions are seen as bright stripes on CL images when we detect at the high energy side of the QW emission peak. This result is further supported by the observation of a perfect contrast inversion on CL images when changing the detection energy from the high energy side, 3.13 eV, to the low energy side, 3.07 eV, of the QW main emission peak.

Since we concluded above that a significant number of dislocations are inside the valleys we may ask about the influence of the valley structure on carrier recombination around dislocations. A TD at the bottom of a valley is surrounded by energetic barriers which might hinder excited carriers from diffusing towards the TD and recombine non radiatively. This gives a possible explanation for the high luminescence efficiency of InGaN/GaN heterostructures: excited carriers do not diffuse towards the TDs in the valleys since they are "self-screened" by potential barriers formed during InGaN growth. This screening hinders excited carriers from non radiative recombination which explains the high luminescence efficiency in spite of high TD densities.

To give a further proof of the above assumption, we have to show that excited carriers effectively diffuse away from the bottom of valleys. We will measure local pTRCL signal by exciting inside valleys and outside valley regions. We expect a pronounced spectral diffusion in function of time towards lower energies inside the valleys compared to the temporal traces from outside the valleys. The spectral diffusion has its origin in the carrier diffusion away from the bottom of the valleys (high energy) to lower energy regions.

3.4.4 pTRCL measurements

On figure 3.22 we depict a streak camera trace when the electron beam is focused at the bottom of a valley (a) and outside the valley (b) of sample B. The excitation point is targeted by looking at a CL image recorded at 3.07 eV (the low energy side of the thin QW luminescence peak) while displacing the sample in the xy-directions using the motorized stage. During targeting the CL image acquisition rate is approximately 10 Hz which can make the task rather difficult due to low contrast between valley and outside valley regions. Once the sample is in position, we use the maximal available magnification of the microscope (300'000 X) and we switch the electron microscope to spot mode (fix position for the electron beam, i.e. no scanning). Then we switch the monochromator output from the PM to the Streak camera which was aligned beforehand. Acquiring a streak trace takes approximately 2 min. Once the acquisition is done, we register a "control" CL image to verify that there was no important sample or beam shift during the measurement. Figure 3.22 shows typical streak camera traces which are treated numeri-

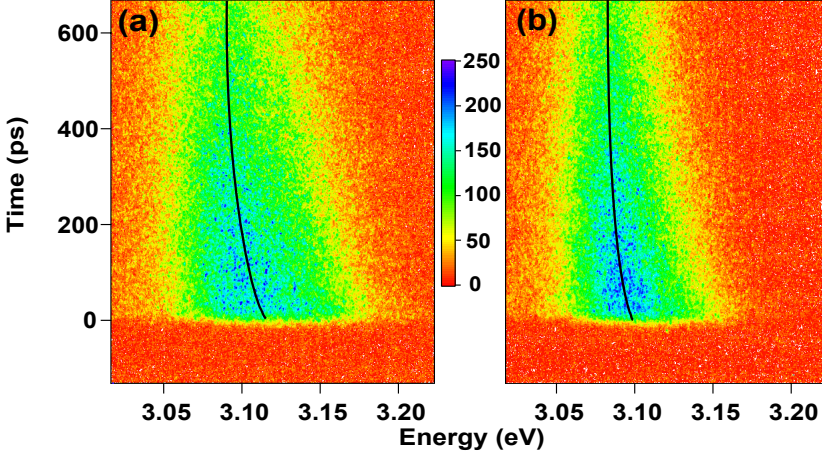


Figure 3.22: Streak camera traces (a) in the valley and (b) outside the valley region. Color coded intensities are in arbitrary units. Black lines are guides to the eye.

cally to be proportional to energy on the horizontal scale. Black lines on the streak camera traces are guides to the eye to evidence the observed spectral diffusion.

When the excitation point is chosen inside a valley (figure 3.22(a)) we observe a very pronounced spectral diffusion of $\approx 80 \text{ meV}$ towards lower energy within 600 ps after excitation. Interestingly, local CL spectra from the valleys have a full width at half maximum (FWHM) of 86 meV compared to a FWHM of 57 meV outside the valley. In order to understand and interpret these results better, we calculated the energy profile of the thin QW as a function of the well thickness (see figure 3.23) extracted from the AFM images on figures 3.18, 3.19(a) and 3.20(a).

3.4.5 Discussion

In order to calculate the electron and hole energy levels we need first to determine the internal electrical field E . This can be done by means of formula

3.18 using only the structural parameters of the sample given in the section sample structure. We find $E = 2100 \text{ kVcm}^{-1}$. From an experimental point of view it might be more realistic to use the following method: We measure by standard photoluminescence (PL) the energy position of the thin QW luminescence peak. We use the method described on page 51-52 and in the Appendix A with the internal electric field E as a variable until the energy position of the QW luminescence peak is reproduced. The thickness of the well is taken to be constant and equal to its nominal thickness, $d = 1.5 \text{ nm}$. This method yields $E = 1800 \text{ kVcm}^{-1}$. To calculate the energy profile of the thin InGaN QW we extract thickness profiles from AFM images along a direction perpendicular to the valleys. In figure 3.23(a) we present AFM

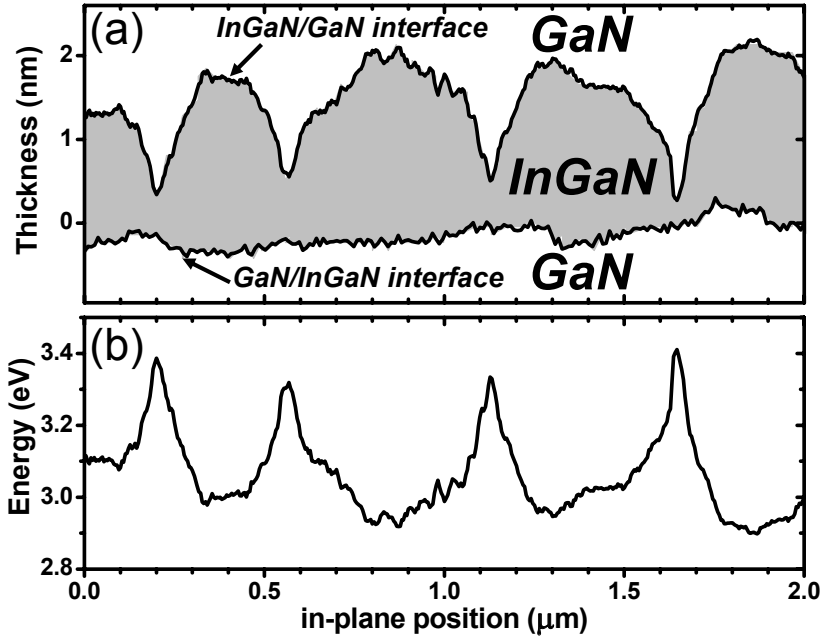


Figure 3.23: (a) AFM profiles and (b) calculated energy profiles for the thin QW. The dotted line represents an averaged energy profile.

section profiles. The first GaN/InGaN interface is extracted from figure 3.18.

The InGaN/GaN cap layer interface is extracted from figure 3.19(a). If we assume that the segregation and the diffusion of the indium atoms in the well is low during the growth, those sections correspond to the two InGaN/GaN interfaces of the QW. The relative position of the two section profiles in figure 3.23 is set so that the total InGaN volume, represented here by the gray surface, stays constant. The total InGaN volume, V_{InGaN} , is given by: $V_{InGaN} = d \times l \times \rho = 1.5 \text{ nm} \times 2 \text{ }\mu\text{m}$ where d is supposed to be the nominal QW thickness, l the distance over which the profiles were extracted and ρ a surface density. It is not necessary to know the absolute value of ρ .

The dark curve in figure 3.23(b) presents the energy variation of the InGaN QW calculated from the profiles on figure 3.23(a). This was determined by using the above described method, an average In composition of $x = 15\%$ and an internal electric field of $E = 1800 \text{ kVcm}^{-1}$. Despite the valley profile of the InGaN QW, we consider that $E = 1800 \text{ kVcm}^{-1}$ represents an average value of the internal field since it was obtained by fitting the energy position of the thin QW luminescence peak in a standard PL measurement. Moreover, the exciton energy of a thin QW is not very sensible to the electric field: the exciton energy of QW with nominal thickness of 1.5 nm only changes by 23 meV when the absolute value of the internal electric field is changed from 1800 kVcm^{-1} to 2200 kVcm^{-1} . For thinner QWs the energy change would be even smaller. This energy variation due to internal field variation influences in no way the argumentation below.

The calculated energy profile inside the valleys shows a variation of $\approx 100 \text{ meV}$ over a distance of $\approx 100 \text{ nm}$. This explains the larger FWHM of the local CL spectra inside the valleys (we measure an increase of $\approx 30 \text{ meV}$) compared to local CL spectra outside valleys: the same number of excited carriers has access to more different energy levels for recombination in the valleys due to the rapidly changing QW thickness. We can also use the widths of the temporal trace from the valley (figure 3.22) to estimate an upper limit of the electron beam diameter arriving on the sample surface: the initial energy width (meaning at zero delay) of the temporal trace indicates the energy spread between energy levels to which excited carriers have access before diffusion. This means that the distance over which this energy spread occurs inside a valley gives an upper limit to the electron probe diameter. We find approximately 50 nm which is in good agreement with our estimated maximal spatial resolution in SE mode.

To be sure that the observed spectral diffusion (redshift) on the streak trace from the bottom of the valley (figure 3.22(a)) can be associated to carrier diffusion we have to be certain that the internal electric field is not screened by the injected carriers. If the injected carrier density is high enough the electric field might be partially screened at short times (compared to the pulse length) after the pulse arrival [57, 58]. Due to the QCSE, this leads to higher recombination energies at the beginning of the signal decay than at its end also signifying a spectral diffusion to lower energies. We have two arguments to show that we do not screen the internal electrical field in our measurements:

1. The effect of the electric field on the luminescence energy of such thin QW is very small. The energy difference between the electric field free case and the case with field is $< 50 \text{ meV}$. Since we observe a spectral diffusion of $\approx 80 \text{ meV}$ this can not only be due to electric field compensation by screening through excited carriers.
2. The excitation density $\rho_{ex} \approx 4 \cdot 10^{11} \text{ cm}^{-2}$ is approximately one hundred times inferior to the calculated screening density (see page 52).

As a consequence, we attribute the observed spectral diffusion to carrier diffusion towards lower energies.

We can thus conclude that carriers created in the vicinity of TDs inside a valley effectively diffuse away from the TDs towards lower energies. As a result, TDs in the valleys are energetically screened by energy barriers induced by the particular growth mode of InGaN. Excited carriers diffuse away from TDs due to the potential profile surrounding them. Carriers no longer recombine non radiatively at dislocations. Thus the energy screening of TDs in the valleys provides an explanation of the high luminescence efficiency of InGaN/GaN optoelectronic devices. Now, we can also try to explain why we do not observe dark spots corresponding to the TDs in CL images recorded at either side of the thin QW luminescence peak. We assume that only the excited carriers that arrive inside the dislocation core recombine non radiatively. Lets suppose that the dislocation core has a diameter of a few nanometers, only about 1 % of the excited carriers recombine non radiatively in the TD core. This would signify a CL contrast variation of 1 % around a

TD which is within the noise in CL measurements.

It is important to mention that the particular morphology we observe of the InGa_N QW has already been observed for MOVPE grown InGa_N QWs [59]. Also the effect of a built-in potential barrier around dislocations was recently proposed by Hangleiter *et al.* [60]. They proposed that V-shaped defects formed by threading dislocations act as potential barriers for carriers. It seems that the effect of "TD self-screening" could be generalized in the present case, where the interplay between TD terminations and step flow growth produces potential barriers leading to carrier localization.

We will estimate the diffusion distance, L_{diff} , of the excited carriers to see whether it is consistent with the observed spectral diffusion (energy shift). Assuming that the movement of the excited carriers is purely diffusive the diffusion distance is given by $L_{diff} = \sqrt{\tau D}$ where τ is the effective lifetime and D the diffusion coefficient of the excited carriers. We assume that the ambipolar diffusion coefficient D for InGa_N well represents the exciton diffusion coefficient. Ambipolar diffusion coefficient was measured by Aleksiejūnas *et al.* [61] for thin InGa_N layers by the transient grating method. Using their value of $D = 2.1 \text{ cm}^2/\text{Vs}$ we find $L \approx 100 \text{ nm}$.

3.5 Conclusion

Bulk GaN

TDs at the surface of bulk GaN can be identified as correlated dark spots in CL imaging mode. In our model we model TDs in GaN as negatively charged line with a cylindrical space charge region around them with diameter L_{dept} . To calculate CL contrast around a dislocation we suppose that all excitons within the space charge region around a TD recombine non radiatively. Fitting contrasts around monochromatic CL images yields an exciton diffusion distance of $L_{diff} \approx 180 \text{ nm}$. Local pTRCL lifetime measurements show most likely an increase in the radiative lifetime of the free exciton luminescence peak when the excitation spot is moved from a dislocation free zone onto a dislocation. This increase can be explained by the separation between the electron and the hole due to the electric field in the space charge region around a TD. On the other hand, we observe a 25% decrease of the effective

lifetime indicating that non radiative recombination becomes most probably predominant when approaching a dislocation. The simple model making use of a space charge region around TDs can not explain the non radiative lifetime changes. Using the measured lifetime we can estimate an exciton diffusion coefficient of $D \approx 4 \text{ cm}^2 \text{ s}^{-1}$ in good agreement with other measures.

In order to gain more detailed information on luminescence lifetimes around TD we plan to do studies on thin GaN samples (microdisks and mechanically thinned samples) and we've done studies on InGaN based QWs.

InGaN QW

We have successfully implemented a double QW structure with a high energy QW at the surface and a lower energy QW far from the surface ("barrier" QW). Thanks to this sample structure we show high resolution in monochromatic CL images of the surface QW.

This allowed correlation of morphological information obtained by AFM measurements with CL measurements of the InGaN QW. The InGaN QW exhibits deep valleys in the $< 1 - 100 >$ directions where the QW thickness almost decreases to zero. We showed that the valley formation is due to the hindering of the InGaN step flow through TDs which induces a surface depression behind them. To further support this result we showed that the valley density diminishes when the TD density decreases. Moreover, we measure a slight disorientation of the (0001) surface of $0.26 \pm 0.02^\circ$ by AFM which is in good agreement with the value given by the substrate supplier.

Due to the thinner well in the valley, luminescence peaks are shifted to high energy in these regions as observed in local CL spectra. A diffusion process is evidenced in InGaN QWs by time resolved CL measurements and a diffusion length L_{diff} of $\approx 100 \text{ nm}$ is extracted. This extracted diffusion length seems to be in good agreement with the observed spectral shift inside the valleys due to carrier diffusion. We show that carriers effectively diffuse away from the bottom of the valleys. This signifies that TDs inside the valleys are energetically screened from non radiative recombination since excited carriers diffuse away from them.

This main result might explain the high luminescence efficiency of InGaN/GaN

based optoelectronic devices despite the high dislocation density, a major puzzle over the last years: excited carriers do not "see" the dislocation since they would have to overcome a potential wall.

4 Boron Nitride

4.1 Introduction

Due to its very high bandgap, estimated around 6 eV , hexagonal boron nitride (hBN) is a promising material for optoelectronic devices including deep UV light emitters. Experimental evidence for deep UV lasing has been published in 2004 by Watanabe *et al.* in Nature [62]. The crystal structure of hBN consists of stacks of two-dimensional hexagonal layers of boron and nitride atoms. Boron Nitride represents a quasi two-dimensional insulator very similar to stacks of graphite sheets. Interest in hBN has been considerably renewed recently by the possibility of rolling up hBN sheets to obtain single- and multiwall nanotubes [63, 64] which are far more resistant to oxidation than carbon nanotubes and therefore suited for high-temperature applications.

In the framework of density-functional-theory local-density-approximation (DFT-LDA) scheme and including the so called GW quasi-particle corrections, sophisticated ab-initio electronic structure and optical spectrum calculations concerning hBN [65, 66] as well as BN nanotubes [67, 68] have been undertaken. There is still a controversy concerning the direct or indirect nature of the hBN fundamental bandgap. Watanabe *et al.* [62] state that since hBN is a very efficient light emitter, the fundamental bandgap is of direct nature and they interpret their near band-gap luminescence peaks in the Wannier exciton scheme (delocalized excitons at the atom scale). Whereas Silly *et al.* [69] explain the near bandgap luminescence peaks in a quasi two-dimensional Frenkel exciton scheme (localized excitons at the atomic scale) and state that the fundamental bandgap is indirect (based on the theoretical results by Arnaud *et al.* [65]).

In collaboration with A. Loiseau and P. Jaffrennou from ONERA, we started to work on hBN. We will present first time-resolved spectra measured on

commercially available hBN powders from Sigma-Aldrich Corp. The next step is to try to measure luminescence lifetime in function of temperature and excitation point on single- and multiwall BN nanotubes. Examination of hBN in the pTRCL setup has at least three important advantages:

1. Since the acceleration voltage of the electrons is typically a few keV , CL is the ideal tool to study wide bandgap semiconductors.
2. The high spatial resolution of the electron microscope is needed to choose the adequate excitation point. SE images and CL images can help identify the structure to study.
3. Luminescence decay time in function of different parameters (like excitation point or temperature) gives important information about fundamental processes in the sample.

Experimental results obtained on the hBN powder will be presented in the next section. Streak traces are obtained using the alternative detection line described in the experimental setup chapter.

4.2 Experimental Results

The samples are cooled to $T = 95\text{ K}$ and we use an acceleration voltage of $V_{acc} = 8\text{ kV}$. Since the alternative detection line is not configured to register monochromatic CL images we use the SE mode of the SEM to target the crystallite we want to investigate. Figure 4.1 shows a SE image of the hBN crystallite under study deposited on an electron microscopy grid. The crystallites have typical diameters reaching from $\approx 3\text{ }\mu\text{m}$ to $15\text{ }\mu\text{m}$. To record time resolved spectra we work at the maximal magnification of the electron microscope ($\times 300'000$) which means that an area of approximately $0.3 \times 0.3\text{ }\mu\text{m}^2$ is scanned on the sample. Figure 4.2 depicts a streak camera trace of the hBN crystallite shown in figure 4.1. The streak camera is used in photon counting mode and measurement times per image are around three minutes. When looking at the time-integrated spectra on figure 4.3 which is extracted from the streak traces on figure 4.2, three well distinguished peaks can be identified: the highest energy and most intense peak is centered at 5.77 eV (215 nm) followed by two less intense peaks at 5.63 eV (220 nm) and 5.46 eV (227 nm). The energy position of these peaks shows that hBN is most likely a high bandgap material with a bandgap around 6 eV . Figure 4.4 depicts the

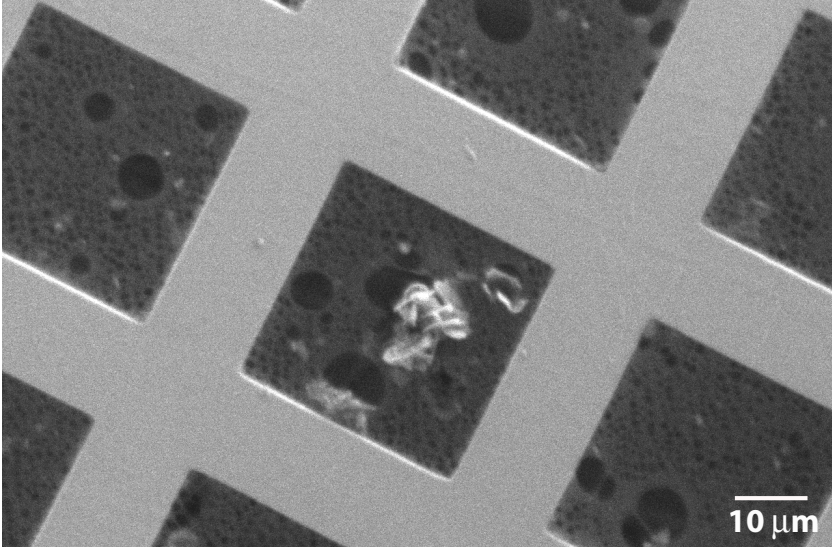


Figure 4.1: SE image of the hBN crystallite under study, $V_{acc} = 8\text{ kV}$ and $T = 95\text{ K}$.

temporal dependency of the three main luminescence peak. These data is also extracted from 4.2. Extraction of the temporal traces is done by integrating over a range of $\approx 93\text{ meV}$ centered at the luminescence peak energy under study. The measured luminescence lifetime does not change when we choose a smaller width for the integration range but the dynamical range of the signal decreases. This is why we chose 93 meV . Interestingly, we observe very short lifetimes. Already 100 ps after excitation the luminescence of the three peaks seems to be completely decayed. Fitting the traces with a monoexponential function yields similar lifetimes of 20 ps , 18 ps , and 32 ps , respectively for the three peaks in decreasing energy order.

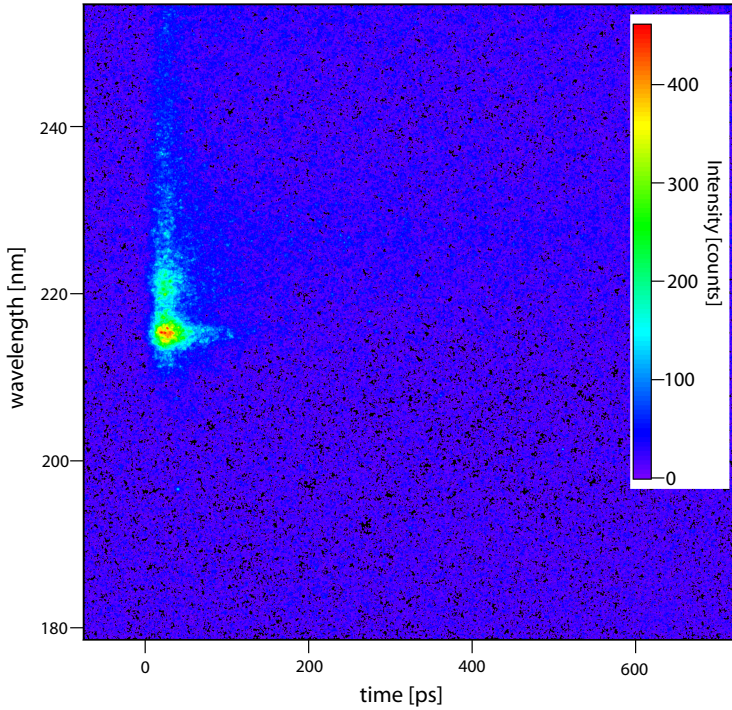


Figure 4.2: Streak camera trace of an hBN crystallite. Intensity is colour coded. See text below for discussion.

4.3 Discussion

Our measures were focused on the hBN near bandgap region and the origin of the three observed luminescence peaks on figure 4.2 can be readily identified as being excitonic in perfect agreement with other measurements and calculations [62, 70, 65]. We also observe the so called blue emission band centered around 4 eV . These transitions, which are not discussed here, have been identified as transitions between impurity levels [62, 69]. We measure effective lifetimes of approximately 1 ns for the blue emission band. By comparing monochromatic CL images, TEM images and SEM images

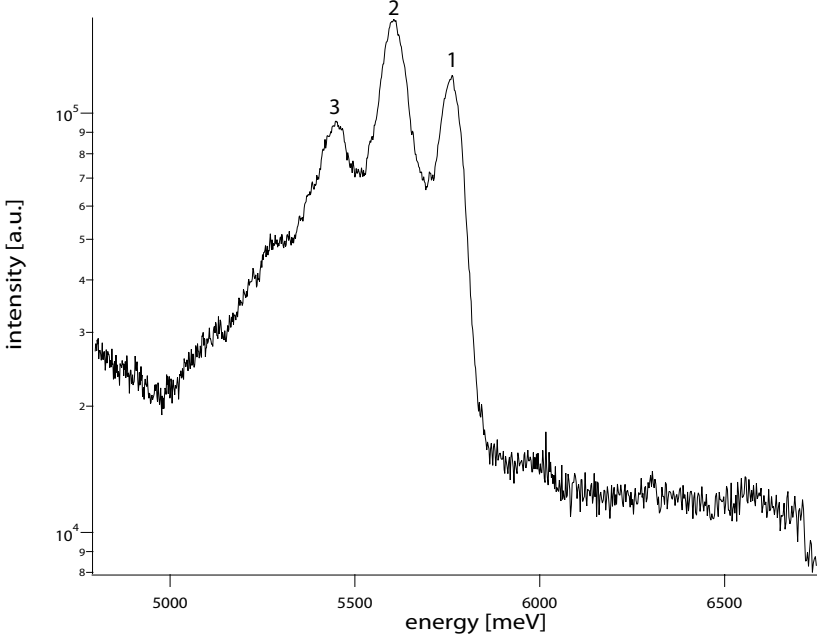


Figure 4.3: CL spectra of hBN. Three peaks marked with 1 (5.77 eV), 2 (5.63 eV) and 3 (5.46 eV) can be clearly distinguished.

of a hBN crystallite, Jaffrennou *et al.* [70] identified the highest energy luminescence peak at 5.77 eV as a free exciton peak. The luminescence peak at 5.63 eV as a structural defect bound exciton and the peak at 5.46 eV as another structural defect bound exciton or as a phonon replica of the peak at 5.63 eV . To unambiguously conclude on the free or bound nature of the excitons we will conduct pTRCL lifetime studies as a function of temperature. To successfully continue these studies we will use the new liquid helium cryostat which is actually being tested. The bound exciton lifetime is expected to be constant with temperature [71].

There have been several ab-initio calculations on the electronic bandstructure of hBN [65, 66] and of hBN nanotubes [67]. The calculations all show that

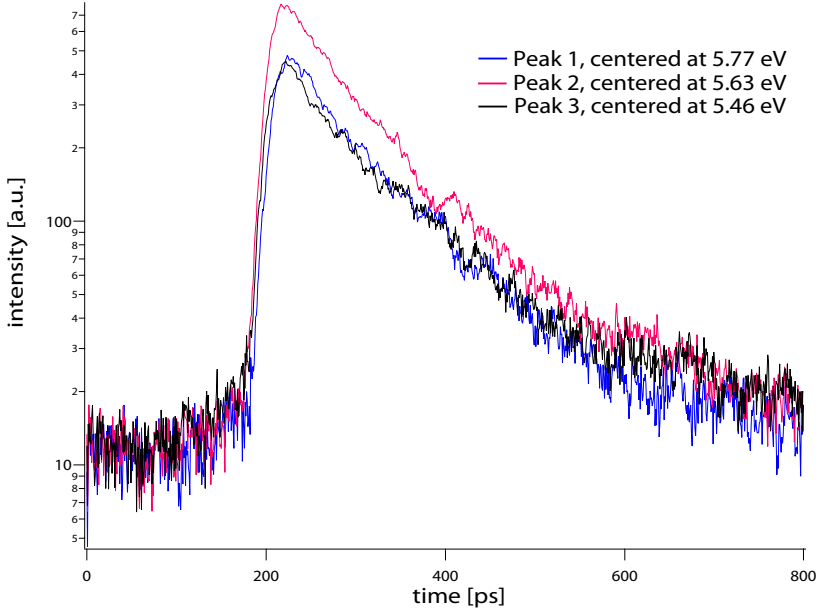


Figure 4.4: Temporal dependency of the three observed luminescence peaks. 1, 2 and 3 correspond to the luminescence peak designation given in figure 4.2.

the minimum gap is of the indirect type in k space. We use the numerical values by Arnaud *et al.* [65] which best fit experimental results, ours as well as others [62, 70]. They find (see figure 4.3) a minimum band gap of 5.95 eV between the minimum of the conduction band at the M point and the maximum of the valence band at the T_1 point (near the K point). The minimum direct bandgap of 6.47 eV is located at the H point.

The short effective lifetimes of the excitonic peaks we measure seem to be in contradiction with the indirect nature of the hBN bandgap. Due to momentum conservation, an indirect exciton needs to interact with phonons before its radiative recombination. Thus one would expect very long radiative lifetimes, typically nanoseconds (see [72] about time-resolved photoluminescence studies in GaP which is an indirect semiconductor). To simplify,

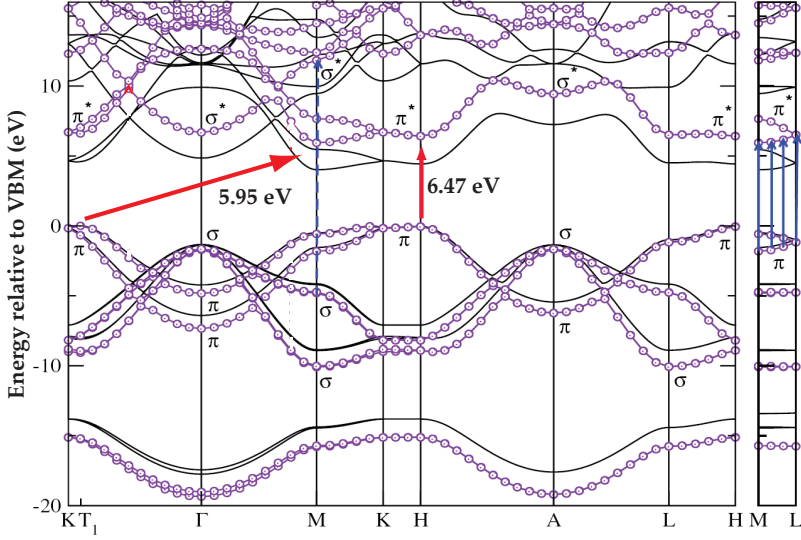


Figure 4.5: Calculated electronic bandstructure along high-symmetry lines for bulk hBN. Energies are relative to the valence band minimum (VBM). The thin solid line shows the LDA results while the circles show the GW results which we refer to in the text. Arrows indicate the fundamental direct and indirect bandgaps. This figure is taken from [65].

lets suppose that the radiative lifetime τ_{rad} equals $\tau_{rad} = 10 ns$ and let's try to estimate the maximum number of created photons through radiative exciton recombination. We take one electron per pulse with an energy of $8 keV$ and we consider that it needs the energy three times the bandgap ($6.57 eV$) to create one electron hole-pair. We create a maximum number of 500 photons per pulse. Since the blue band is approximately 40 times more intense than the excitonic band [70], we consider that only 10 photons originate from excitonic recombination. If all these photons get extracted from the sample we collect only about 3 of them limited by the solid angle covered by the parabolic mirror. Distributed over $\tau_{rad} = 10 ns$, such a signal is not

detectable with the streak camera since the longest time window for signal acquisition (timerange) is 2 ns . Since we clearly detect a signal on the streak camera we think that τ_{rad} is considerably shorter than 10 ns . Thus we follow Arnaud *et al.* and interpret the exciton nature as being direct and of the Frenkel type, despite the indirect minimum bandgap, at the H point which accounts for the short lifetimes. This result is further supported by the high calculated oscillator strength (compared to other possible transitions) for the excitonic states.

We also have to consider that non radiative channels might be very efficient and thus limit the effective lifetime. To conclude about this issue one would need to measure the internal quantum efficiency of the sample.

By measuring time resolved luminescence spectra of hBN bulk crystallites we have demonstrated the utility of the pTRCL setup for deep UV applications extending to energies as high as 5.77 eV (215 nm). Furthermore we observe three excitonic luminescence lines in agreement with other measurements [70]. By estimating the maximum number of photons produced per electron pulse, we conclude that the excitons are of direct type despite the indirect nature of the fundamental gap of hBN. To our knowledge, this is the first observation of effective exciton lifetimes as short as 18 ps in an indirect semiconductor. Ongoing studies will definitely conclude on the free or bound character of the observed excitons. Furthermore we plan to do in-depth studies of multi- and singlewall isolated BN nanotubes.

5 Conclusions and perspectives

5.1 pTRCL Setup

We describe the performance and the working principle of the pTRCL setup. This unique setup is characterized by **combined** spatial and temporal resolutions of 50 nm and 12 ps , respectively. These characteristics make it an ideal tool to study semiconductor based nanostructures, including high bandgap materials. The xyz precision displacement system brings an important improvement to the setup since controlled sample positioning becomes possible. Two photon excitation of the gold photocathode and pulsed secondary electron detection are briefly discussed. These two methods will be implemented in the setup during the next months. We've also received a new liquid helium cryostat developed in collaboration with Janis, Inc. which is currently under test.

We successfully mounted and tested an alternative detection line using a monochromator based on an achromatic UV objective. This detection line is easy to use and signal loss is lower than with the standard detection line.

5.2 GaN and InGaN QW

After a brief review of the fundamental parameters of GaN and InGaN we first present luminescence lifetime measurements on bulk GaN. TDs are interpreted as non radiative recombination centers and we show a 25% decrease of luminescence lifetime when displacing the excitation spot from dislocation free bulk material onto a dislocation. This result indicates that non radiative recombination most probably become predominant when approaching a dislocation.

To do high resolution CL, we grew a double QW with a high and a low energy QW. The low energy acts as an energetic barrier hindering excited carriers from diffusing to the high energy well thus deteriorating CL resolution. Interestingly, we do not observe any contrast due to TDs when we

detect monochromatic CL on the high energy well. For the TDs inside the valleys this is most probably due to the carrier diffusion away from dislocations. This means that only excited carriers directly on the dislocation core recombine non-radiatively. Assuming a core diameter of a few nanometer, the number of excited carriers which recombine non-radiatively directly at the TD core is very small compared to the total number of excited carriers which signifies that the contrast difference between on and off dislocation measurement is too small to be detected with our resolution. We observe a contrast inversion between monochromatic CL maps corresponding to the high energy side (3.13 eV) and the low energy side (3.07 eV) of the QW luminescence peak. In perfect correlation with CL images, AFM images clearly show regions where the QW thickness almost decreases to zero.

Pronounced spectral diffusion from high energy thinner regions to low energy thicker regions is observed in picosecond TRCL, providing an explanation for hindering of non-radiative recombination at dislocations. This main result gives a possible explanation of the high luminescence efficiency of In-GaN/GaN based optoelectronic devices, a major puzzle over the last years.

In order to better understand recombination mechanism around dislocation we are conducting ongoing studies on thinned samples and on microdisks. The idea of both kinds of samples is to have a maximal spatial resolution in CL imaging by maximally reducing the interaction volume of the primary electrons with the structure under study.

5.3 Boron Nitrides

We've demonstrated the utility of the pTRCL setup for deep UV applications as far as 5.77 eV (215 nm) by performing time resolved CL measures on hBN crystallites. We observe three excitonic lines (in accordance with other measures) with very short lifetimes (20 ps, 18 ps and 32 ps). We interpret this excitons as being of direct nature and of the Frenkel type despite the indirect fundamental bandgap of hBN.

We will conduct lifetime studies as function of temperature to conclude about the free or bound nature of the excitons. The goal of the studies on BN is to measure luminescence lifetimes of excited carriers in single wall BN nan-

otubes. So far we have managed to measure very faint signal from multiwall BN nanotube. The idea of the ongoing experiments is to characterize the nanotubes by TEM measurements in order to be able to distinguish between single and multi wall nanotubes. Once the TEM characterization is done, we will study the same nanotubes by pTRCL.

5.4 Perspectives

We have developed a, to our knowledge, unique measurement tool to characterize nanostructures yielding combined spatial and temporal resolution of 50 nm and 12 ps respectively. We are entirely convinced that the pTRCL setup is and will be a very valuable tool to study transport properties and local luminescence properties of semiconductor based nanostructures. Furthermore, there might be other new applications like integrated circuit testing. In this field, our tool could become a very important failure detection instrument since the present integrated circuit technology goes already down to 45 nm .

The use of electron pulses instead of a continuous electron beam might also be advantageous to avoid sample charging which is an important problem for samples presenting bad electrical conductivity. In between the pulses, additional charges on the sample might evacuate even on a bad conductor. From the technical point of view, the performances of the setup can be considerably enhanced. The temporal resolution is presently limited by space charge effects at the cathode level. It is however possible to produce single electrons already at the cathode level which would greatly improve temporal resolution [73]. There are reports, for example the one by Hommelhoff *et al.* [74], about single electron generation by 8 fs laser pulses which predicts electron pulse lengths of 1 fs . Such a time resolution would open doors to investigate a wealth of new phenomena. Spatial resolution should also be improved if we worked with single electrons already at the cathode level.

Based on these motivation and perspectives, the author, with another EPFL colleague, launched a startup company with the goal to commercialize and further develop the pTRCL technique. This new venture was launched under the name Attolight (www.atto-light.com). The project won the Venture Leader Prize 2007 founded by the Gebert-Rüf Stiftung and we received pre-seed financing which allows to pay salaries during the first year of activity.

Presently, the main focus of Attolight concentrates on market survey and on finding first customers. Attolight's Business Model is based on sales and service. By service we understand sample characterization for third parties which we do on our prototype at EPFL in order to familiarize and confide customers to our new technique.

Bibliography

- [1] R. P. Leavitt, and J. W. Little. *Physical Review B*, 42:11774, 1990.
- [2] M. Merano, S. Sonderegger, A. Crottini, S. Collin, P. Renucci, E. Pelucchi, A. Malko, M. H. Baier, E. Kapon, B. Deveaud, and J. D. Ganière. *Nature*, 438(24):479, 2005.
- [3] M. Merano, S. Sonderegger, A. Crottini, S. Collin, P. Renucci, E. Pelucchi, A. Malko, M. H. Baier, E. Kapon, J. D. Ganière, and B. Deveaud. *Applied Physics B - Lasers and Optics*, 84:343, 2006.
- [4] S. Nakamura, T. Mukai, and M. Senoh. *Applied Physics Letters*, 64:1687, 1994.
- [5] M. Merano. *Picosecond Cathodoluminescence*. PhD thesis, Ecole Polytechnique Federale de Lausanne, 2005.
- [6] P. Vernier, E. Coquet, and E. Boursey. *Czech. Journal of Physics B*, 19:918, 1969.
- [7] M. Merano, S. Collin, P. Renucci, M. Gatri, S. Sonderegger, A. Crottini, J. D. Ganière, and B. Deveaud. *Review of Scientific Instruments*, 76:085108, 2005.
- [8] H. Ihee, V. A. Lobastov, U. M. Gomez, B. M. Goodson, R. Srinivasan, C.-U. Ruan, and A. H. Zewail. *Science*, 291:458, 2001.
- [9] M. Y. Schelev, G. I. Bryukhnevich, V. I. Lozovoi, M. A. Monastyrski, A. M. Prokhorov, A. V. Smirnov, and N. S. Vorobiev. *Opt. Eng. (Bellingham)*, 37:2249, 1998.
- [10] J. Cao, Z. Hao, H. Park, C. Tao, D. Kau, and L. Blaszczyk. *Appl. Phys. Lett.*, 83:1044, 2003.
- [11] R. Clauberg and A. Blacha. *J. Appl. Phys.*, 65:4095, 1989.

- [12] S. Collin, M. Merano, M. Gatri, S. Sonderegger, P. Renucci, J.-D. Ganière, and B. Deveaud. *J. Appl. Phys.*, 98:094910, 2005.
- [13] T. Srinivasan-Rao, J. Fischer, and T. Tsang. *J. Appl. Phys.*, 69:3291, 1990.
- [14] Reiner Burgschat. Optoelektronische Sensoren für die Weg- und Winkelmessungen. *Numerik Jena GmbH*.
- [15] Ch. Palmer. *Diffraction grating handbook*. Richardson Grating Laboratory, 4th edition, 200.
- [16] I. Vurgaftman, J. M. Meyer, and L. R. Ram-Mohan. *Appl. Phys. Rev.*, 89:5815, 2001.
- [17] J. F. Nye,. *Physical Properties of Crystals, Their Representation by Tensors and Matrices*. Clarendon Press, Oxford, 2004.
- [18] Ursula M. E. Christmas, A. D. Andreev, and D. A. Faux. *Journal of Applied Physics*, 98:073522, 2005.
- [19] O. Ambacher, J. Majewski, C. Miskys, A. Link, M. Hermann, M. Eickhoff, M. Stutzmann, F. Berardini, V. Fiorentini, V. Tilak, B. Schaff, and L. F. Eastman. *Journal of Physics: Condensed Matter*, 14:3399, 2002.
- [20] F. Bernardini, V. Fiorentini, and D. Vanderbilt. *Physical Review B*, 63:193201, 2001.
- [21] F. Bernardini, V. Fiorentini, and D. Vanderbilt. *Physical Review B*, 56:R10024, 1999.
- [22] T. Takeuchi, S. Sota, M. Katsuragawa, M. Komori, H. Takeuchi, H. Amano, and I. Akasaki. *Japanese Journal of Applied Physics, Part 2*, 36:L382, 1997.
- [23] P. Lefebvre, A. Morel, M. Gallart, T. Taliercio, J. Allègre, B. Gil, H. Mathieu, B. Damilano, N. Grandjean, and J. Massies. *Applied Physics Letters*, 78:1252, 2001.
- [24] S. L. Chuang and C. S. Chang. *Physical Review B*, 54:2491, 1996.

-
- [25] S. L. Chuang and C. S. Chang. *Semiconductor Science and Technology*, 12:252, 1997.
- [26] M. Leroux, N. Grandjean, B. Beaumont, G. Nataf, F. Semond, J. Massies, and P. Gibart. *Journal of Applied Physics*, 86:3721, 1999.
- [27] E. Kornitzer, T. Ebner, M. Grehl, K. Thonke, R. Sauer, C. Kirchner, V. Schwegler, M. Kamp, M. Leszczynski, I. Grzegory, and S. Porowski. *Physica Status Solidi (b)*, 216:5, 1999.
- [28] S. J. Rosner, E. C. Carr, M. J. Lusowise, G. Girolami, and H. I. Erikson. *Applied Physics Letters*, 70:420, 1997.
- [29] Y. Yamamoto, H. Itoh, V. Grillo, S. F. Chichibu, S. Keller, J. S. Speck, S. P. DenBaars, U. K. Mishra, and S. Nakamura. *Journal of Applied Physics*, 94:4315, 2003.
- [30] S. Dassonneville, A. Amorkane, B. Sieber, J.-L. Farvaque, B. Beaumont, and P. Gibart. *Journal of Applied Physics*, 89:3736, 2001.
- [31] T. Sugahara, H. Sato, M. Hao, Y. Naoi, S. Kurai, S. Tottori, K. Yamashita, K. Nishino, L. T. Romano, and S. Sakai. *Japanese Journal of Applied Physics*, 37:L398, 1998.
- [32] F. Calle, F. J. Sánchez, J. M. G. Tijero, M. A. Sánchez-Garcia, E. Calleja, and R. Beresford. *Semiconductor Science and Technology*, 12:1396, 1997.
- [33] Y. P. Varshni. *Physica*, 34:149, 1967.
- [34] W. Shan, T. J. Schmidt, X. H. Yang, S. J. Hwang, J. J. Song, and B. Goldenberg. *Physical Review Letters*, 66:985, 1995.
- [35] W. Shan, B. D. Little, A. J. Fisher, J. J. Song, B. Goldenberg, W. G. Perry, M. D. Bremser, and R. F. Davis. *Physical Review B*, 54:16369, 1996.
- [36] J. Szczytko, L. Kappei, J. Berney, F. Morier-Genoud, M. T. Portella-Oberli, and B. Deveaud. *Physical Review Letters*, 93:137401, 2004.
- [37] M. Colocci, M. Gurioli, and A. Vinattieri. *Journal of Applied Physics*, 68:2809, 1990.

- [38] D. Robart, X. Marie, B. Baylac, T. Amand, M. Brousseau, G. Bacquet, G. Debart, R. Planel, and J. M. Gerard. *Solid State Communications*, 95:287, 1995.
- [39] W. A. Brantley, O. G. Lorimor, P. D. Dapkus, S. E. Hasko, and R. H. Saul. *Journal of Applied Physics*, 46:2629, 1975.
- [40] E. Müller, D. Gerthsen, P. Brückner, F. Scholz, Th. Gruber, and A. Waag. *Physical Review B*, 73:245316, 2006.
- [41] J. Cai and F. A. Ponce. *Physica status solidii (a)*, 192:407, 2002.
- [42] D. Cherns and C. G. Jiao. *Physical Review Letters*, 87:205504, 2001.
- [43] D. Cherns, C. G. Jiao, H. Mokhtari, J. Cai, and F. A. Ponce. *Physica status solidii (b)*, 234:924, 2002.
- [44] M. Abramowitz and I. A. Stegun,. *Handbook of Mathematical Functions*. Dover Publications, Inc., 9th edition, 1972.
- [45] J. Mickevičius, M. S. Shur, R. S. Qhalid Fareed, J. P. Zhang, R. Gaska, and G. Tamulaitis. *Applied Physics Letters*, 87:4241918, 2005.
- [46] N. Pauc, M. R. Philips, V. Aimez, and D. Drouin. *Applied Physics Letters*, 89:161905, 2006.
- [47] B. Damilano, N. Grandjean, J. Massies, L. Siozade, and J. Leymarie. *Journal of Applied Physics*, 77:1268, 2000.
- [48] J.-M. Bonard. *Etude par microscopie électronique des propriétés structurales et optiques de laser à semi-conducteur*. PhD thesis, Ecole Polytechnique Federale de Lausanne, 1996.
- [49] D. A. B. Miller, D. S. Chemla, T. C. Damen, A. C. Gossard, W. Wiegmann, T. H. Wood, and C. A. Burrus. *Physical Review Letters*, 53:2173, 1984.
- [50] F. Bernardini, V. Fiorentini. *Physica status solidii (b)*, 216:391, 1999.
- [51] V. Fiorentini, F. Bernardini, F. Della Salla, A. di Carlo, and P. Lugli. *Physical Review B*, 60:8849, 1999.

-
- [52] V. Fiorentini, F. Bernardini, and O. Ambacher. *Applied Physics Letters*, 80:1204, 2002.
- [53] F. Bernardini, V. Fiorentini. *Physical Review B*, 64:085207, 2001.
- [54] D. S. Chemla, T. C. Damen, D. A. B. Miller, A. C. Gossard, W. Wiegmann. *Applied Physics Letters*, 42:864, 1983.
- [55] S. Dalmaso. *Mécanisme d'injection de de recombinaison radiatives et non-radiatives dans les diodes électroluminescentes à base de nitrures d'éléments III*. PhD thesis, Université de Nice-Sophia Antipolis, 2001.
- [56] N. Grandjean, E. Feltin, R. Butté, J.-F. Carlin, S. Sonderegger, B. Deveaud, and J.-D. Ganière. *Philosophical Magazine*, 78:2067, 2007.
- [57] T. Takeuchi, S. Sota, M. Katsuragawa, M. Komori, H. Takeuchi, H. Amano, and I. Akasaki. *Japanese Journal of Applied Physics*, 36:L382, 1997.
- [58] T. Kuroda and A. Tackeuchi. *Journal of Applied Physics*, 92:3071, 2002.
- [59] S. M. Ting, J. C. Ramer, D. I. Florescu, V. N. Merai, B. E. Albert, A. Parekh, D. S. Lee, D. Lu, D. V. Christini, L. Liu, and E. A. Armour. *Journal of Applied Physics*, 94:1461, 2003.
- [60] A. Hangleiter, F. Hitzel, C. Netzel, D. Fuhrmann, U. Rossow, G. Ade, and P. Hinze. *Physical Review Letters*, 95:127402, 2005.
- [61] R. Aleksiejūnas, M. Sūdžius, V. Gudelis, T. Malinauskas, K. Jarašiūnas, Q. Fareed, R. Gaska, M. S. Shur, J. Zhang, J. Yang, E. Kuokštis, and M. Khan. *Phys. Status Solidi C*, 7:2686, 2003.
- [62] K. Watanabe, T. Taniguchi, and H. Kando. *Nature materials*, 3:404, 2004.
- [63] A. Loiseau, F. Willaime, N. Demoncy, G. Hug, and H. Pascard. *Physical Review Letters*, 76:4737, 1996.
- [64] N. G. Chopra, R. J. Luyken, K. Cherrey, V. H. Crespi, M. L. Cohen, S. G. Louie, and A. Zettl. *Science*, 269:966, 1995.
- [65] B. Arnaud, S. Lebègue, P. Rabiller, and M. Alouani. *Physical Review Letters*, 96:026402, 2006.

- [66] X. Blase, A. Rubio, S. G. Louie, and M. L. Cohen. *Physical Review B*, 51:6868, 1995.
- [67] L. Wirtz, A. Marini, and A. Rubio. *Physical Review Letters*, 96:126104, 2006.
- [68] C.-H. Park, C. D. Spataru, and S. G. Louie. *Physical Review Letters*, 96:126105, 2006.
- [69] M. G. Silly, P. Jaffrennou, J. Barjon, J.-S. Lauret, F. Ducastelle, A. Loiseau, E. Obraztsova, B. Attal-Tretout, and E. Rosencher. *Physical Review B*, 75:085205, 2007.
- [70] P. Jaffrennou, J. Barjon, J.-S. Lauret, B. Attal-Tretout, F. Ducastelle, and A. Loiseau. *submitted to Applied Physics Letters*, 2007.
- [71] J. Bellessa, V. Voliotis, R. Grousson, X. L. Wang, M. Ogura, and H. Matsuhata. *Physical Review B*, 58:9933, 1998.
- [72] I. A. Buyanova, G. Pozina, J. P. Bergmann, W. M. Chen, H. P. Xin, and C. W. Tu. *Applied Physics Letters*, 81:52, 2002.
- [73] M. S. Grinolds, V. A. Lobastov, J. Weissenrieder, and A. H. Zewail. *Proceedings of the National of Sciences of the United States of America*, 103:18427, 2006.
- [74] P. Hommelhoff, C. Keahofer, and M. A. Kasevich. *Physical Review Letters*, 97:247402, 2006.
- [75] G. Bastard. *Wave mechanics applied to semiconductor heterostructures*. Les éditions de physique, 1988.

A Calculation methods

A.1 The transfer matrix method to evaluate hole and electron envelope functions in a QW

We suppose that the states are described by a single band envelope functions f_i^e and f_j^h where i and j are the subband indices and e and h design electron and hole respectively. The states are described by the following Schrödinger equations:

$$\left[\frac{-\hbar^2}{2} \frac{d}{dz_e} \left(\frac{1}{m_e} \frac{d}{dz_e} \right) + V_e(z_e) \right] f_i^e = E_i^e f_i^e(z_e), \quad (\text{A.1})$$

for electrons and

$$\left[\frac{-\hbar^2}{2} \frac{d}{dz_h} \left(\frac{1}{m_{h\perp}} \frac{d}{dz_h} \right) + V_h(z_h) \right] f_j^h = E_j^h f_j^h(z_h) \quad (\text{A.2})$$

for holes where m_e and $m_{h\perp}$ are the electron and hole effective masses in direction normal to the QW layers (parallel to the [0001] direction). The effect of the internal electric field E_{int} is included in the potentials $V_e(z_e)$ and $V_h(z_h)$. Inside the QW these potentials are given by:

$$V_e(z_e) = V_{0,CB} + eE_{int}z_e \quad (\text{A.3})$$

$$V_h(z_h) = V_{0,VB} + eE_{int}z_h \quad (\text{A.4})$$

where $V_{0,CB}$ and $V_{0,VB}$ are the conduction and valence band offsets between the well and barrier materials respectively.

The growth axes, z , is divided into steps of length Δz so that the potentials $V_{0,CB}$ and $V_{0,VB}$ can be considered constant over Δz . In each slab Δz the solution to the Schrödinger equation (with constant potential) is a plane wave

of the form $\phi = Ae^{ikz} + Be^{-ikz}$ where k is the wavevector. The confinement energy in the QW is determined by the continuity of the wavefunctions when passing from one slab to another and by the conservation of the probability current [75]:

$$\phi_i(z_i) = \phi_{i+1}(z_i) \quad (\text{A.5})$$

$$\frac{1}{m_i^*} \frac{d}{dz} \phi_i(z_i) = \frac{1}{m_{i+1}} \frac{d}{dz} \phi_{i+1}(z_i) \quad (\text{A.6})$$

where i ($1 \leq i \leq N$) numbers the slabs of thickness Δz and m_i^* is the respective effective mass. The coefficients A_{i+1} and B_{i+1} can be connected to A_i and B_i through the *transfer matrix* M_i :

$$\begin{pmatrix} A_{i+1} \\ B_{i+1} \end{pmatrix} = \begin{pmatrix} \frac{1}{2}(1+\alpha)e^{i(k_i-k_{i+1})z_i} & \frac{1}{2}(1-\alpha)e^{-i(k_i+k_{i+1})z_i} \\ \frac{1}{2}(1-\alpha)e^{i(k_i-k_{i+1})z_i} & \frac{1}{2}(1+\alpha)e^{-i(k_i+k_{i+1})z_i} \end{pmatrix} \begin{pmatrix} A_i \\ B_i \end{pmatrix} \quad (\text{A.7})$$

where $\alpha = \frac{m_{i+1}^*}{m_i^*} \frac{k_i}{k_{i+1}}$. The above system (equation A.7) can be formulated in function of the starting vector, (A_1, B_1) and the end vector (A_N, B_N) :

$$\begin{pmatrix} A_N \\ B_N \end{pmatrix} = \begin{pmatrix} M_{11}(E) & M_{12}(E) \\ M_{21}(E) & M_{22}(E) \end{pmatrix} \begin{pmatrix} A_1 \\ B_1 \end{pmatrix} \quad (\text{A.8})$$

where E is the energy of the electron or hole. Choosing $B_N = 0$ and $A_1 = 0$ avoids exponential divergence of the wavefunctions at the border. Energy levels are determined by $M_{22}(E) = 0$. The wavefunctions are determined by starting with $(A_1 = 1, B_1)$ and by evaluating the transfer matrix in every slab with the corresponding energy. Finally, the wavefunctions are normalized: $\int \phi^2(z) dz = 1$.

A.2 Calculation of the Excitonic Rydberg [1]

Once the electron and hole envelope functions are known, the exciton binding energy, Ry , is given by the following explicit formula [1]:

$$Ry = \int_{-\infty}^{\infty} dz_e dz_h |f_i^e(z_e)|^2 |f_j^h(z_h)|^2 E_0 w(v), \quad (\text{A.9})$$

where $E_0 = \mu_{\parallel} e^4 / 2\epsilon^2 \hbar^2$ and $\mu_{\parallel} = m_e^* m_{h\parallel}^* / (m_e^* + m_{h\parallel}^*)$ with m_e^* the electron effective mass and $m_{h\parallel}^*$ the hole effective mass in a plane parallel to the QW layer. The function $w(v)$ is given by:

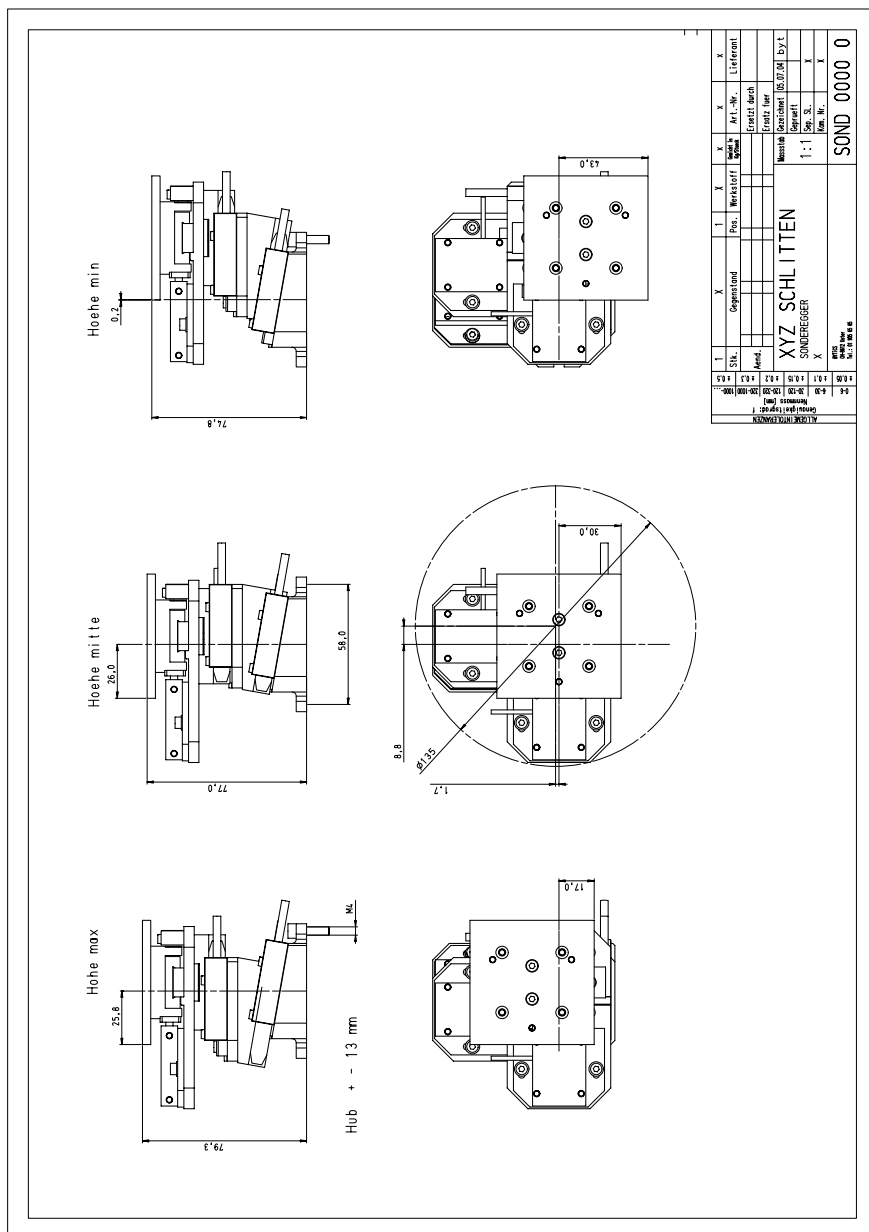
$$w(v) = \frac{4 + c_1 v + c_2 v^2}{1 + d_1 + d_2 v^2 + d_3 v^3}, \quad (\text{A.10})$$

with $c_1 = 12.97$, $c_2 = 0.7180$, $d_1 = 9.65$, $d_2 = 9.24$, and $d_3 = 0.3706$.

B Technical drawings

B.1 Technical drawings of the xyz precision displacement system

B.2 Technical drawing of the achromatic UV objective



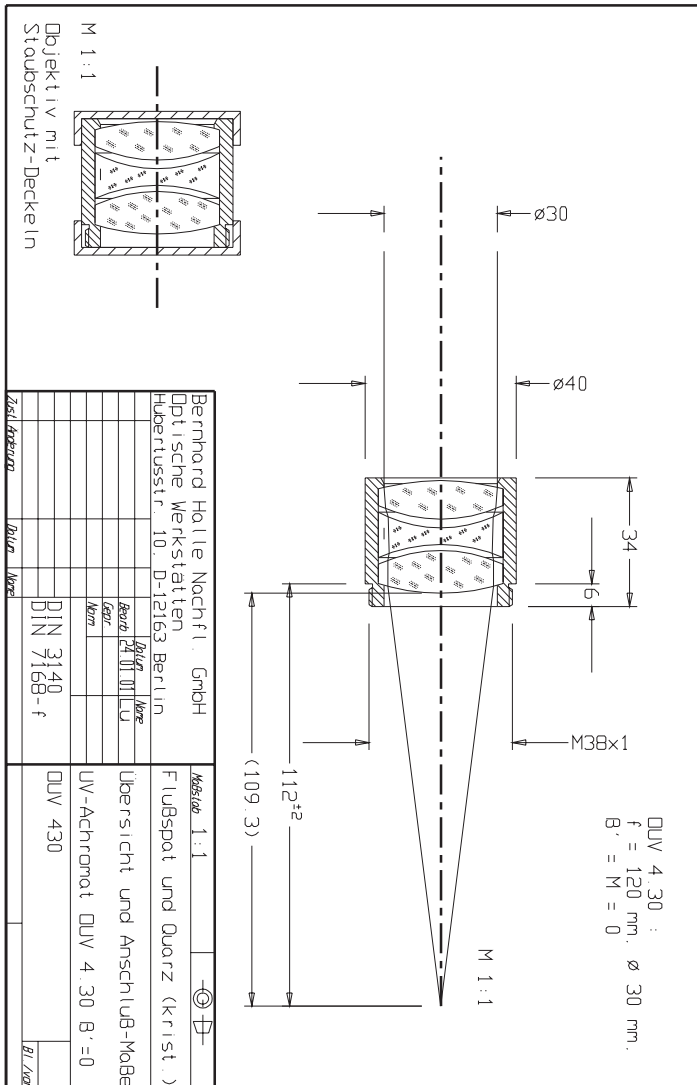


Figure B.2: Technical drawings of the achromatic UV objective.

List of publications and attended conferences

List of publications in refereed journals

1. N. Grandjean, E. Feltin, R. Butté, J.-F. Carlin, **S. Sonderegger**, B. Deveaud, and J.-D. Ganière, "Growth mode induced carrier localization in InGaN/GaN quantum wells", invited paper, Philosophical Magazine, **87**(13), 2067 (2007).
2. **S. Sonderegger**, E. Feltin, M. Merano, A. Crottini, J.-F. Carlin, R. Sachot, B. Deveaud, N. Grandjean, and J.-D. Ganière, "High spatial resolution picosecond cathodoluminescence of InGaN quantum wells", Applied Physics Letters, **89**, 232109 (2006).
3. M. Merano, **S. Sonderegger**, A. Crottini, S. Collin, E. Pelucchi, P. Renucci, A. Malko, M. H. Baier, E. Kapon, J.-D. Ganière, and B. Deveaud, "Time-resolved cathodoluminescence of InGaAs/AlGaAs tetrahedral pyramidal quantum structures", invited paper, Applied Physics B-Laser and Optics, **84**, 343 (2006).
4. M. Merano, **S. Sonderegger**, A. Crottini, S. Collin, P. Renucci, E. Pelucchi, A. Malko, M. H. Baier, E. Kapon, B. Deveaud and J.-D. Ganière, "Probing carrier dynamics in nanostructures by picosecond cathodoluminescence", Nature, **438**, 479 (2005).
5. M. Merano, S. Collin, P. Renucci, M. Gatri, **S. Sonderegger**, A. Crottini, J.-D. Ganière, and B. Deveaud, "High brightness picosecond electron gun", Review of Scientific Instruments, **76**(8), 085108 (2005).
6. S. Collin, M. Merano, M. Gatri, **S. Sonderegger**, P. Renucci, J.-D. Ganière, and B. Deveaud, "Transverse and longitudinal space-charge-induced broadenings of ultrafast electron packets", Journal of Applied Physics, **98**(9), 094910 (2005).

List of talks at attended conferences

ICNS6-International conference on nitride semiconductors

Bremen, August 28th - September 2nd 2005

15min talk "Picosecond cathodoluminescence to study GaN structures".

OECS9-Optics of Excitons in confined systems

Southampton, September 3th - September 10th 2005

15min talk "Probing carrier dynamics of nanostructures by picosecond cathodoluminescence".

BYTICS Tagung: Ganz gross im Kleinsten

Uster, March 22nd 2005

30min invited talk "XYZ stage in (Hoch)Vakuumanwendungen".

Swiss Physical Society (SPS) 2006 Meeting,

Lausanne, February 13th - 14th 2006

15min talk "Picosecond time resolved cathodoluminescence to study GaN structures".

Summer School on Wide-Bandgap Semiconductors

MonteVerita, Switzerland, August 27th - September 1st 2006

Poster presentation "High spatial resolution picosecond cathodoluminescence of InGaN quantum wells".

IWN06, International workshop on nitride semiconductors

Kyoto, Japan, October 22nd - October 27th 2006

15min talk "High spatial resolution picosecond cathodoluminescence of InGaN quantum wells".

ICNS7, International conference on nitride semiconductors

Las Vegas, USA, September 16th - September 21st 2007

15min talk "Luminescence Lifetime in the Vicinity of Threading Dislocations

on Bulk GaN Studied by Picosecond Time Resolved Cathodoluminescence".

Curriculum Vitae

SAMUEL SONDEREGGER

EPFL SB IPEQ LOEQ
PH D2 399, station 3
CH-1015 Lausanne

29 ans
Suisse

FORMATION

- 2003 - présent **Thèse de doctorat** à l'*Ecole Polytechnique Fédérale de Lausanne (EPFL)* dans le domaine de la caractérisation spectroscopique des nanostructures.
- 2003 **Diplôme d'Ingénieur Physicien** à l'*EPFL*.
- 2000 - 2001 **Echange académique** à l'*Ecole Normale Supérieure de Lyon 1*.

Stages de Management :

- 2006 **Venture Challenge (5 mois)**. Cours d'entrepreneuriat organisé par *VentureLab*. Projet d'entreprise Attolight sélectionné comme sujet d'étude parmi 20 projets.
- 2006 **Cours de négociation (3 jours)**. Organisé par l'*EPFL*.

PRIX

- 2007 **Venture Leader**. Vainqueur du concours pour jeunes entrepreneurs financé par la *Gebert Rûf Stiftung*.
- 2007 **INNOGRANT**. Obtention d'une bourse pour le lancement de l'entreprise Attolight.

PROJETS

- 2006 - présent **Start-up Attolight**. Commercialisation d'un outil de mesure perfectionné durant ma thèse.
- 2005 - présent **Supervision de la construction d'un cryostat** pour un microscope électronique à balayage (MEB).
- 2004 **Construction d'un système de déplacement de précision (6 mois)** pour un MEB. Collaboration avec BYTICS AG, Uster, Suisse.
- 2002 **Travail de diplôme** au *IOFFE Institute* à *St. Pétersbourg* dans le domaine de la physique des semiconducteurs.
- 2001 **Projet d'ingénieur (2 mois)** à l'*Université de Lyon 1* dans le domaine de la détection et de la caractérisation des aérosols.